2010

The effects of chamber pressure variation on swirl injector atomization

Chad Jonathan Eberhart

THE EFFECTS OF CHAMBER PRESSURE VARIATION ON SWIRL INJECTOR ATOMIZATION

by

CHAD JONATHAN EBERHART

A THESIS

Submitted in partial fulfillment of the requirements
for the degree of Master of Science in Engineering
in
The Department of Mechanical and Aerospace Engineering
to
The School of Graduate Studies
of
The University of Alabama in Huntsville

HUNTSVILLE, ALABAMA

2010

In presenting this thesis in partial fulfillment of the requirements for a master's degree from The University of Alabama in Huntsville, I agree that the Library of this University shall make it freely available for inspection. I further agree that permission for extensive copying for scholarly purposes may be granted by my advisor or, in his/her absence, by the Chair of the Department or the Dean of the School of Graduate Studies. It is also understood that due recognition shall be given to me and to The University of Alabama in Huntsville in any scholarly use which may be made of any material in this thesis.

Chad Jonathan Eberhart

28 July 2010
(date)

THESIS APPROVAL FORM

Submitted by Chad Jonathan Eberhart in partial fulfillment of the requirements for the degree of Master of Science in Engineering in Aerospace Engineering and accepted on behalf of the Faculty of the School of Graduate Studies by the thesis committee.

We, the undersigned members of the Graduate Faculty of The University of Alabama in Huntsville, certify that we have advised and/or supervised the candidate of the work described in this thesis. We further certify that we have reviewed the thesis manuscript and approve it in partial fulfillment of the requirements for the degree of Master of Science in Engineering in Aerospace Engineering.

Robert A Frederick 7/28/10
Dr. Robert A. Frederick, Jr. (Date) Committee Chair

7/28/2010
Dr. David M. Lineberry (Date)

Marlow D Moser 28 July 2010
Dr. Marlow D. Moser (Date)

7/29/10
Dr. A. Kader Frendi (Date) Department Chair

7/30/10
Dr. Phillip A. Farrington (Date) College Dean

Rhonda Kay Gaede 11/23/10
Dr. Rhonda Gaede (Date) Graduate Dean

ABSTRACT

School of Graduate Studies
The University of Alabama in Huntsville

Degree Masters of Science in Engineering College/Dept. Engineering/Mechanical and Aerospace Engineering

Name of Candidate Chad Jonathan Eberhart

Title The Effects of Chamber Pressure Variation on Swirl Injector Atomization

This body of work presents a unit physics investigation into the fundamental fluid mechanics of a single liquid rocket swirl injector element. In an effort to correspond with sub-scale combustion experiments, an assessment of spray structure and atomization was conducted as a function of steady-state chamber conditions. A cold flow experimental methodology was applied, whereby flow of liquid oxygen was simulated with de-ionized H_2O. The geometrically full-scale element was tested at chamber pressures ranging from 0.95-3.46 MPa (152.2-500 psia) — correlating with expected characteristic exhaust velocity-efficiency values of 0.38-1.4. Over all tests, mass flow rate was held constant at the element's design point, 0.082 $\frac{kg}{s}$ (0.181 $\frac{lb_m}{s}$). Within this range of conditions, images of the spray were captured, and through objective analyses, qualitative and quantitative measurements of several spray features were resolved. To assess self-atomizing characteristics, Phase Doppler Particle Analysis experiments were conducted. Droplet velocity and diameter measurements were mapped to capture a spatial representation of droplet flow behavior across the spray envelope.

Abstract Approval: Committee Chair

Dr. Robert A. Frederick, Jr.

Department Chair

Dr. A. Kader Frendi

Graduate Dean

Dr. Rhonda Gaede

ACKNOWLEDGMENTS

The direction and support afforded by my committee members was critical to the successful completion of this work. Firstly, Dr. Robert Frederick administered the academic guidance necessary for an undertaking of this type; gratitude must be extended to him for providing the opportunity to conduct research under his tutelage. Secondly, Dr. Marlow Moser rendered the technical and theoretical insight largely responsible for the success of the experimentation. His hands-on laboratory expertise was instrumental to this work. Lastly, the numerous contributions of Dr. David Lineberry must be addressed; from day one, his impact on the design of the experimental facility and analysis of results was significant. His council dramatically influenced the course of this research for the better.

The work ethic of the Propulsion Research Center's staff is reflected in this research. From thought-provoking conversation to the simple lending of a helping hand, support from students and staff was tremendous. Particularly, the assistance of Mr. Tony Hall and Mr. Craig Morris was invaluable to the construction of the experimental facility. Furthermore, Mr. Matthew Wilson is deserving of acclaim for his excellent partnership through the testing phase of the investigation.

The support provided by my family and those I hold dear was unwavering. Through the various struggles and successes, their nurture and inspiration were steadfast. In regard to this research, many parameters were readily quantified, but the most elusive of all was the value of such personal support — it remains immeasurable.

TABLE OF CONTENTS

PAGE

LIST OF FIGURES

FIGURE **PAGE**

LIST OF TABLES

TABLE **PAGE**

LIST OF SYMBOLS

SYMBOL	DEFINITION
A	**droplet surface area**
A_t	**nozzle throat area**
b	**systematic uncertainty**
c	**linear calibration y-intercept**
c_e^*	**experimental characteristic exhaust velocity**
c_t^*	**theoretical characteristic exhaust velocity**
D_p	**particle diameter**
d_{10}	**mean diameter**
d_{30}	**volume mean diameter**
d_{32}	**Sauter mean diameter**
d_{in}	**tangential inlet diameter**
d_n	**nozzle diameter**
d_{vc}	**vortex chamber diameter**
Da,i	**First Damköhler group**
Da,iii	**Third Damköhler group**

ΔP	**pressure differential**
E	**output voltage**
Fr	**Froude number**
f/	**lens aperture**
h	**film thickness**
L	**length**
L_{in}	**tangential inlet length**
L_{vc}	**vortex chamber length**
M	**Mach number**
MW_{poc}	**product of combustion molecular weight**
m	**mass**
$\dot{m}$	**mass flow rate**
N	**characteristic number**
P	**pressure**
PR	**pressure ratio**
Pr	**Prandtl number**
q	**linear calibration slope**
R_u	**universal gas constant**

$\boldsymbol{Re}$	**Reynolds number**
$\boldsymbol{Sc}$	**Schmidt number**
s	**random uncertainty**
T	**temperature**
t	**time**
U	**total uncertainty**
u	**sheet axial velocity**
V	**velocity**
$\forall$	**droplet volume**
$\boldsymbol{We}$	**Weber number**
We_a	**aerodynamic Weber number**
x	**horizontal coordinate**
z	**vertical coordinate**

Greek

α	**light scatter parameter**
β	**transition angle**
Γ	**ratio of specific heats**
γ	**surface tension**
Δ	**fringe spacing**

η	**characteristic exhaust velocity efficiency**
θ	**free cone spray angle**
κ	**sheet penetration length**
λ	**incident photon wavelength**
μ	**dynamic viscosity**
ν	**t-distribution number**
π	**3.14159**
ρ	**density**
σ	**standard deviation**
τ_i	**chemical conversion time**
ϕ	**equivalence ratio**

Subscripts

a	**axial component**
c	**chamber**
f	**focal**
g	**gas phase**
l	**liquid phase**
n	**nozzle**
r	**radial component**

v venturi

CHAPTER 1

INTRODUCTION

1.1 Background

A demand for enhanced technological efficiency, coupled with increased fiscal constraint, has led the contemporary liquid rocket propulsion community to implement computational fluid dynamics (CFD) in the aid of engine design. No longer can a full-scale "build and test" strategy be practiced in the development of liquid propellant rocket engines (LPREs), rather engine conditions are often simulated with CFD on an *a priori* basis to the assembly and testing of physical hardware. Such modern numerical efforts require a fidelity that's scope includes the capture of, amongst others, combustion thermochemistry, turbulent fluid dynanics, heat transfer, and acoustics. With the multitude of mechanisms at work, and the interactions between these mechanisms, it is often elusive to fully realize LPRE performance, stability, and heat transfer phenomena with computational methods.

Since direct numerical simulation of such flows is, as of yet, still infeasible, a practical unit physics approach has been taken to enhance the

breadth of CFD simulations that support liquid rocket engine design. Focus has been placed on understanding fundamental physical mechanisms; the understanding of these mechanisms yields advanced models of processes. Process models can then be integrated together to better understand and predict phenomena within, and performance of, LPRE combustors.

To support such a design approach, the practice of device scaling becomes an important tool. In place of full-scale testing, device scaling calls upon archived test data and sub-scale experiments of LPRE components to complement CFD. Experimental data on component behavior and performance are the crux of a CFD design approach. By verifying simulation results with observations and measurements, experimental data serves to anchor numerical predictions in reality. Furthermore, boundary conditions for the Navier-Stokes system of equations are gathered from experimental data.

The critical nature of sub-scale component testing becomes apparent when put into context with the device scaling and CFD design approach. Compared to full-scale testing, sub-scale experiments often require significantly less capital. The ability to perform sub-scale experiments in a laboratory setting reduces development cost in two manners: the reduction of test hardware cost and the reduction of test personnel and maintenance [1]. For the past quarter-century, considerable research effort has been con-

certed to study sub-scale combustion devices in the federal, private, and academic arenas.

Within the realm of sub-scale combustor testing, appreciable interest lies in understanding the energy release characteristics of injector elements: atomization, mixing, vaporization, and reaction. Typical sub-scale experiments emphasize the study of uni-element combustors to identify engine efficiency, often on merit of characteristic exhaust velocity (c^*) comparison. These types of experiments can provide some measure of vaporization and heat release characteristics associated with the reaction of propellants, but the combustion physics' chemical conversion time scale (τ_i) dominates over the time scales associated with injection fluid mechanics. It is in this regard that sub-scale hot fire combustion experiments offer reduced insight towards the atomization and mixing energy release characteristics of an injector element.

1.2 Approach

To thoroughly examine injector flow fields, the fluid mechanics of injection must be removed from phenomenological events that occur within real combustors. For assessment at steady state conditions, it is desirable to eliminate the chamber pressure perturbations and acoustic field-to-spray interactions that result from combustion instabilities. One solution is to separate the injection process from the combustion process, alto-

gether. Such separation nullifies the τ_i of the combustion reactions, permitting the examination of energy release characteristics associated with fluid mechanics. However, these processes are not necessarily de-coupled from the reaction. Gas expansion and turbulence of the reaction may impart additional aerodynamic effects on injection and atomization [2].

Additionally, the isolation of injector flow from the combustion reaction extends benefit to experimental procedures. The physical manifestations of the combustion process — excessive heat release and light radiation — are avoided. Independent of these manifestations, an environment with enhanced optical access to injector fluid mechanics can be developed, a test bed conducive to non-intrusive laser diagnostic and imaging experiments.

To meet the requirements of such injector fluid mechanics examinations, a cold flow methodology must be implemented. Permitting the study of processes such as atomization and propellant mixing, cold flow testing is a common construct to injector experimentation. A cold flow test bed can accommodate the flow of combustible liquid and gaseous propellants, but to promote a non-reactive environment, propellant fluids are often replaced with simulants. To preserve flow similarity, the use of a propellant simulant requires the fluid properties to match those of the real propellant.

Although a simulant does not require complete fidelity to an actual propellant, matching of certain fluid properties are specific to the flow

Table 1.1: Fluid Thermophysical Properties

Fluid	T (K)	ρ ($\frac{kg}{m^3}$)	γ ($\frac{N}{m}$)	μ (Pa-s)
LOX	90	1146	$13.2x10^{-3}$	$2.00x10^{-4}$
LN_2	90	751	$6.09x10^{-3}$	$1.06x10^{-4}$
H_2O	273.16	1001	$75.6x10^{-3}$	$17.9x10^{-4}$

behavior of interest. In the evaluation of multi-phase flow, relative surface tension can be a driving fluid property to match. For the study of continuum flow, similarity of density and viscosity are often the drivers. Operating conditions also exert influence on the selection of a simulant. Although surface tension becomes negligible at supercritical conditions, the matching of surface tension can be crucial at subcritical conditions.

De-ionized H_2O can be employed as a simulant for liquid oxygen (LOX) on the basis of density similarity — where at a reasonably assumed injection temperature of 90 K, LOX density is near that of H_2O at standard-temperature-and-pressure. Although the viscosity between H_2O and LOX is dissimilar, the Reynolds number (*Re*) of injection is sufficiently high enough to invoke the assumption of inviscid flow. Table 1.1 contains the fluid properties at P =1.90 MPa for LOX and the two most commonly used LOX simulants: H_2O and liquid nitrogen (LN_2).

There exists an additional approach to simulant selection that does not rely on the similarity of fluid properties, as touched on above with the discussion on *Re*. In this approach, non-dimensional parameters of

cold flow simulant flows are matched to those of real flows. Pertinent to atomization studies, the similarity of Weber number (We) is often most important. Based on droplet diameter similarity, to even approach matching We between LOX and H_2O atomization, either surface tension of the H_2O needs be decreased by approximately an order of magnitude or flow velocity increased by $\approx \sqrt{10}$, as evidenced by Table 1.1.

1.3 Review of Literature

A bounty of cold flow injector research is available in the open literature. Pertinent to the objectives of this research, experimental work has been conducted since the mid 1980's, but in limited quantity. Similar spray studies in the areas of air-breathing propulsion and internal combustion engines are well established. In these regards, research has been under way since the 1930's and is considered to be a mature field of science. Although much data exist for these applications, there is a need for additional research that reflects operational LPRE engine conditions.

1.3.1 Scaling Methodologies

The practice of combustor scaling is defined as "the ability to design new combustion devices with predictable performance on the basis of test experience with old devices" [3]. As an analysis tool, scaling can be implemented in two distinct fashions - combustion scaling and performance scaling. Combustion scaling relies on the relation of numerous

similarity parameters between sets of combustion data. The aerothermochemistry similarity parameters include the Schmidt (Sc), Prandtl (Pr), Mach (M), and Froude (Fr) Numbers, Re, and, additionally, the First & Third Damköhler Groups (Da,i) (Da,iii).

Performance is another merit on which combustors are scaled. In terms of the definition of scaling, performance scaling not only applies on the basis of test experience with old devices, but also experimental data gathered for new devices. In this regard, the focus of many sub-scale combustion device experiments is to provide data for performance scaling. Of the several features to impart influence on the scaling of combustor performance, the magnitude of the injector element's contribution is the largest. Injection characteristics are linked to heat transfer, ignition, and combustion instability. Hence, sub-scale testing of injectors is of particular importance [1].

Two methods are common to performance scaling and govern the way in which sub-scale combustor experiments are physically designed. The method of photo-scaled injector elements proportionally decreases the size of a full-scale injector with that of the subscale combustion chamber. If chamber pressure is to remain constant, injection velocity must increase via an increase in mass flow rate. Thus, the Re of the injector element is not conserved between the full-scale element and the sub-scale element.

Another common performance scaling method is that of identical injector elements. In this case, the geometry of a full-scale injector remains

constant. An injector is tested within a smaller combustion chamber-scaled based on length. Since the geometry of the element is left unchanged, its energy release characteristics remain the same between the full-scale and sub-scale devices. Importantly, the ***Re*** of the injector is conserved [1].

1.3.2 Cold Flow Spray Studies

Relevant to the selection of propellant simulants for cold flow studies, the work of Cox [4] is an important example. In the characterization of shear-coaxial SSME injector elements, several fluids were tested in an effort to simulate LOX flow. Measurements to assess atomization were conducted at a chamber pressure condition of 3.8 MPa and at full-scale operational mass flow rates. It was observed that the use of H_2O as a simulant did not influence the effectiveness of the experiments.

Focus was placed on utilizing flow visualization techniques to capture spray features such as free cone spray angle and sheet penetration length as a function of chamber pressure in this present study. Kenny [5] investigated the effects of chamber pressure on free cone spray angle at ambient chamber pressure and at 4.83 MPa. This work outlined valuable methodologies for the objective analysis of spray images. Both subjective and objective image analysis techniques revealed that spray angle decreased as chamber pressure increased [5] [6]. In their study of the effect of nozzle recess on dual-swirl injection, Kim et al. [7] examined sheet

penetration length as a function of *We* at ambient back pressure. For a single swirling spray with no nozzle recess, sheet penetration length was found to decrease from 70 mm to 40 mm as *We* increased over a range of 100 to 900.

Another initiative of this present body of work was to spatially quantify atomization by mapping droplet velocities and diameters within the primary atomization region of the spray; the effects of chamber pressure on the atomization process are explored. Strakey et al. [8] performed similar work while comparing shear coaxial to swirl coaxial injector elements. Measurements of gas-phase axial velocity and droplet volume mean diameter (d_{30}) were made at different axial locations downstream of the injection plane. The velocities of the spray's smallest droplets were assumed to be indicative of the gas-phase velocity. At each axial location, velocity decreased as radial position increased. Furthermore, as axial location increased, corresponding velocity measurements at radial positions generally decreased. A decrease of d_{30} with an increasing radial distance was also discerned. Measurements of droplet axial velocity of a swirl coaxial injector by Long et al. [9] corresponded to those of Strakey et al. Additionally, Long et al. observed Sauter mean diameter (d_{32}) to increase as radial position increased through the spray.

1.4 Objective

The objective of this research is to investigate the effects of steady chamber pressure on the spray behavior and atomization of an LPRE swirl injector element. Steady-state chamber pressure conditions will be maintained to simulate conditions encountered during uni-element combustion experiments. Mass flow rate will be held constant at the injector's nominal design point.

Qualitative characterization of global spray behaviors will be conducted in an objective manner. The angle at which the swirling spray is issued from the injector nozzle, the free cone spray angle (θ) will be measured via image analysis. Additionally, image analysis techniques will be used to objectively assess the downstream length at which the spray's conical sheet remains intact, the sheet penetration length (κ).

Quantitative assessment of the spray's self-atomizing behavior will be conducted; the shear flow of the injector's outer fuel annulus will be neglected. Phase Doppler Particle Analyzer experiments will measure the axial and radial components of droplet velocity. Mean diameter (d_{10}) and d_{32} of droplets will also be measured by PDPA. Furthermore, count distribution measurements of droplet diameter will be gathered.

CHAPTER 2

FACILITY DECRIPTION & DIAGNOSTIC TECHNIQUES

2.1 The Propulsion Research Center Spray Facility

To conduct experiments and gather measurements required for this study, a controlled laboratory environment was designed and constructed. A spray facility was created in High Bay 1 at the Johnson Research Center Laboratory to accommodate a wide variety of experiments in the characterization of liquid rocket injector element behaviors. Employing air as a gaseous propellant simulant and H_2O as a liquid propellant simulant, the Propulsion Research Center Spray Facility provides a cold flow test bed that isolates the fundamental fluid mechanics of spray injection from the excessive thermal and visible light radiation associated with a liquid rocket combustion environment.

The High Pressure Spray Facility (HiPSF) is a pneumatically driven facility designed to simulate chamber pressure and propellant mass flow conditions experienced within real liquid rocket thrust chambers. Figure 2.1 illustrates the Propulsion Research Center HiPSF. A piping and

Figure 2.1: Propulsion Research Center HiPSF

instrumentation diagram, as well as an associated component list of the facility can be found in Appendix A.

2.1.1 Spray Chamber

The HiPSF revolves around the delivery of liquid and gaseous propellant simulants to test articles located within the HiPSF's spray chamber. Experiments can be conducted within the spray chamber at up to 4.24 MPa (614.7 psia). The 452.7 mm (18 inch) internal diameter and 1.96 m (77 inch) length of the chamber is of full scale thrust chamber geometry. A diagram of the spray chamber is featured in Figure 2.2.

The spray chamber features four 152.4 mm (6 inch) diameter view ports. The view ports house borosilicate windows that provide access for spray visualization and non-intrusive laser diagnostics. Furthermore, each

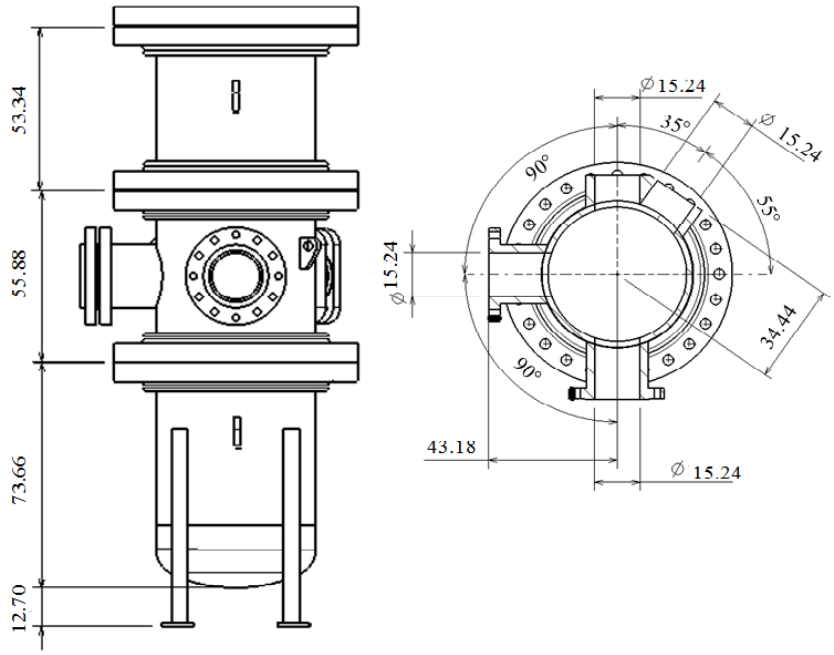

Figure 2.2: HiPSF Spray Chamber Profile (units in cm)

window is equipped with an air spray ring to deter droplet formation on the window surface.

Through the spray chamber wall, three pipe fitting ports enable simulant delivery to a test article. Each simulant has a dedicated port, and a third port accommodates curtain flow to a test article. Curtain flow serves to reduce droplet recirculation zones near the outside boundaries of a spray.

The spray chamber is also outfitted with a dual axis translating stage assembly to provide test article mobility during experiments. Each axis stage is controlled by an independent stepper motor; each motor has a $1.8°$ resolution. Additionally, the lead screw pitch for each axis is **3.94** $\frac{turns}{cm}$.

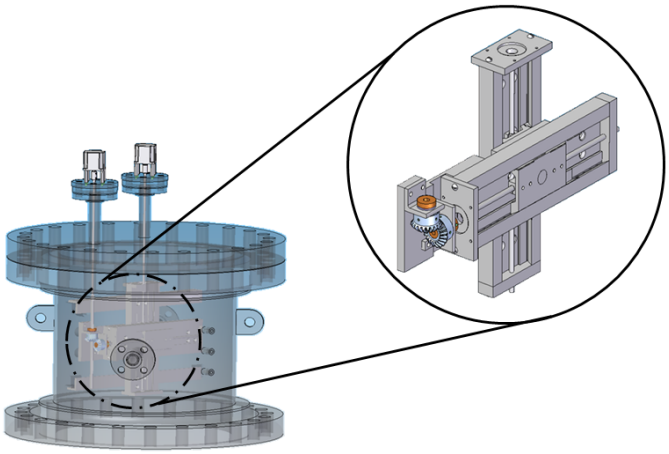

Figure 2.3: Dual-axis Translation Stage within Chamber Head Module

These parameters yield a spatial resolution of approximately $6.35x10^{-3}$ mm in both the horizontal and vertical directions. An illustration of the translating stage assembly is seen in Figure 2.3.

2.1.2 Air Supply System

The HiPSF operates on the Johnson Research Center's Air Supply System. The Air Supply System's compressor maintains the 14.16 kL (3740 gallon) tank at up to 17.34 MPa (2514.7 psia). The Air Supply System provides pressurant to a total of five HiPSF subsystems: valve actuation, liquid simulant delivery, gaseous simulant delivery, and window/curtain flow. While the valve actuation subsystem requires only static pressure, the remaining four subsystems present dynamic pressure requirements. Simulant delivery requirements based on typical liquid rocket engine conditions placed considerable constraints to the system's design.

Viscous compressible (Fanno) flow analyses were performed in an effort to properly identify lines sizes and meet flow requirements. Resulting, the Air Supply System design is capable of providing a theoretical maximum total gas mass flow rate of $\approx 2.36\frac{kg}{s}$ (**5.2** $\frac{lb_m}{s}$) to the HiPSF. The air supply system provides flow to the HiPSF's main bank, from which all subsystems of the facility derive dynamic and/or static pressure.

2.1.3 Valve Actuation Subsystem

The valve actuation subsystem's master hand regulator reduces pressure from the HiPSF total system pressure to static levels suitable for solenoid valve function. The reduced pressure feeds a network of solenoid valves; the solenoid network controls the facility's various pneumatic ball valves. The valve actuation subsystem's pressure is further reduced by an additional micro hand regulator. The micro hand regulator provides static pressure to the fractional flow control valves of the simulant removal subsystem.

2.1.4 Gasesous Simulant Delivery Subsystem

The HiPSF employs air as a gaseous propellant simulant. The gaseous simulant delivery system feeds off of the main air supply bank, whereby a hand regulator/dome-loaded pressure regulator combination controls the dynamic pressure of simulant flow throughout the facility. A fixed orifice venturi meters gaseous simulant mass flow rate to the spray

chamber. The orifice diameter is sized for a desired flow rate, and easily inserted and changed out of the gaseous simulant flow path as per particular test conditions. Flow of gaseous simulant is initiated or ceased by pneumatic ball valve control.

2.1.5 Window/Curtain Flow Subsystem

Separate flow paths are derived from a single window/curtain flow subsystem to delivery air flow, in different capacities, through the HiPSF. The window/curtain flow subsystem employs a hand regulator/dome-loaded pressure regulator combination to reduce pressure from the main air supply bank and to control the dynamic pressure to window flow and curtain flow. The subsystem's flow path is split so that individual needle valves can meter air to a test article's curtain flow or to the high pressure spray chamber's window spray rings. Pneumatic ball valve actuation initiates flow to the windows and the curtain flow.

2.1.6 Water Filtration & Storage Subsystem

To control purity, the facility's liquid propellant simulant is processed through a water filtration and storage subsystem. Firstly, common tap water is passed through a five-stage inline filtration unit. Tap water enters the unit, whereby the initial stage filters sediment from the water. Next the water is transported through a dual-stage NH_2Cl carbon filter. From the carbon filters, the water is finally processed through a dual-stage

deionization system. After processing, the liquid simulant is then stored in a 1893 L (300 gallon) holding tank. Liquid simulant is transported to the liquid simulant delivery subsystem via electric pump.

2.1.7 Liquid Simulant Delivery Subsystem

The liquid simulant delivery subsystem can supply up to 1.36 $\frac{kg}{s}$ (3 $\frac{lb_m}{s}$) of liquid simulant throughout the spray facility. The subsystem consists of pressure regulation devices, a 227 L (60 gallon) run tank, and flow control devices that direct liquid simulant flow. A hand regulator/dome-loaded pressure regulator combination controls the dynamic pressurization of liquid simulant within the run tank; pressures of up to 13.89 MPa (2014.7 psia) can be obtained and sustained within the run tank.

The mass flow rate of liquid simulant is actively controlled by an inline variable area cavitating venturi. The adjustability of the device, in conjunction with pressure control, allows precision liquid simulant metering to a test article. Additionally, the cavitation functionality of the venturi prevents reverse propagation of downstream flow perturbations beyond the throat of the venturi.

The liquid simulant delivery subsystem features several flow loops. The primary loop leads to the high pressure spray chamber. An auxiliary loop directs flow to the Atmospheric Spray Facility (ASF). Flow of the liquid simulant is initiated or ceased by a pneumatic ball valve.

2.1.8 Simulant Evacuation Subsystem

The draining and venting of the spray chamber is actively controlled to maintain a constant pressure control volume in accordance with the conservation of mass. To attain such control, fractional flow control valves are implemented to regulate both chamber pressure and liquid flow exiting the chamber. Proportional-integral-derivative (PID) controllers establish feedback loops of pressure/voltage information with the fractional flow control valves. The fractional flow control valves ensure that liquid simulant and chamber gas are removed at a rate that maintains steady chamber pressure.

2.1.9 Atmospheric Spray Facility

The ASF is an auxiliary liquid simulant flow path that provides controlled flow to test articles in an easily accessible environment. The ASF accommodates check out testing of experimental procedures before implementation in the spray chamber. Additional hardware permits set up of experimental techniques to gather baseline data prior to conduction of elevated chamber pressure experiments.

2.1.10 Control Center

The HiPSF is controlled and operated from the High Bay 1 Control Center. The control center houses a switch panel, programmable logic controller (PLC), and PID controllers to operate the individual HiPSF

subsystems. To isolate the functionality of the facility's flow hardware from software failure, PLC control is implemented on all pneumatic pressurization and vent valves.

The facility's data acquisition (DAQ) system is also located within the control center. Pressure transducer and thermocouple terminals feed into a BNC DAQ card, which, in turn, networks with the DAQ PC card. Via graphical interface, LabView software interacts with the DAQ hardware to gather pertinent pressure, temperature, and mass flow rate measurements. For system control purposes, LabView software also monitors various system pressures throughout the facility. Additionally, LabView software provides control of the translating stage assembly.

2.2 Flow Visualization & Imaging Techniques

Imaging is a crucial diagnostic in the study of spray fluid mechanics. As quoted by Dr. Marlow Moser, "You can learn a lot by looking." An image of a spray can provide tremendous physical insight, and detailed examination can provide useful qualitative information. Furthermore, image analyses can be performed to make quantitative measurements of global spray behaviors.

With the advent of camera sensors that employ complimentary metal-oxide-semiconductors (CMOS) or charged-coupled devices (CCD), many of chemical photography's traditional limitations have been overcome. Nu-

merous digital imaging techniques and lighting schemes can be applied to view sprays in a variety of ways, each offering a unique glimpse of different spray structures.

2.2.1 Backlit

Backlit imaging of a subject requires a light source to be positioned 90° from a subject. A camera is then positioned 180° from the light source. A backlit technique is implemented when the imaging of high boundary contrast is desired. A large lens aperture setting is typically used to limit the amount of light that is gathered by the camera sensor. Furthermore, backlit imaging is advantageous when it is desired to view the averaged movement of a fluid. To capture temporally "steady" images, exposure time is controlled by diminishing the shutter speed.

2.2.2 Stroboscopic

The use of a stroboscopic light source serves to effectively decrease image exposure time. The stroboscope's flash illuminates an object for only a fraction of the time the shutter is open, serving to freeze the motion of the object. To achieve such an effect, the flash frequency of the stroboscope must be matched with the exposure frequency of the imaging device. The increased temporal response afforded by the use of a stroboscope makes this technique attractive when a single image of a rapid

event or unsteady feature is desired. Typical to this technique, a small lens aperture permits an increased quantity of light to reach the sensor.

2.2.3 High Speed Imaging

Although stroboscopic imaging provides temporal responses that allow a snapshot view of unsteady features, the image capture rates of most mechanically and electronically shuttered CMOS or CCD cameras can limit the time scale over which the behavior of such features can be observed in secession. Special high speed cameras, with augmented processing capability and shutter techniques, are used to capture sequential images that can be integrated into a video of an event. With these capabilities, video of both backlit and stroboscopic imaging can be captured, instead of only a single image.

Often, ambient light provided through a fully open lens aperture is not sufficient to illuminate a subject when capturing images at high rates and low exposure times. To exploit the maximum capabilities of a high speed imaging device, elevated levels of light intensity must be provided. Alternative light schemes, such as laser sheeting, are often applied. A delicate balance between frame rate, exposure time, aperture size, and light intensity must be struck.

2.3 Phase Doppler Particle Analysis

A Phase Doppler Particle Analyzer (PDPA) is an instrument which exploits the processes of laser interferometry and light scattering to gather flow measurements in a non-intrusive manner. For the characterization of injector sprays, a PDPA is the critical technology for enabling the measurement of droplet velocities and diameters without disturbing the natural behavior of the flow. To understand how such measurements are collected, it is important to first understand the fundamental processes on which a PDPA functions.

2.3.1 Fundamentals

Applied to the study of optics, the principle of superposition states that when two light waves encounter one another, the net amplitude of the combined waveform is the sum of the individual amplitudes. The phenomenon of interference occurs when two coherent waves of near identical frequency are superimposed. If the sum of the two waves creates a waveform of larger amplitude, the interference is defined as constructive. Constructive interference arises if the individual waves are in phase with each other. Destructive interference occurs when two waves subtract to produce a waveform of lesser amplitude. A phase difference between the individual waves is the root of destructive interference.

Figure 2.4: Interference Pattern Produced by Beam Intersection [10]

When two coherent laser beams intersect, an interference pattern can be observed. Figure 2.4 illustrates a typical fringe pattern. Equation 2.1 describes an interference pattern's fringe spacing (Δ), where λ is the wavelength and N is the number of nodal lines. The application of laser interferometry as a measurement technique is enabled by the ability to identify Δ.

$$\Delta = \frac{\lambda}{2N} \tag{2.1}$$

Light scattering is a basic physical process in which a photon, traveling on a linear trajectory through a uniform medium, is made to deviate from its course upon the encounter of an irregularity in the medium. The size of an irregularity and the wavelength of the incident photon (λ) are used to describe the manner in which light is scattered (α), as seen in Equation 2.1. An irregularity's geometry is typically assumed to be spherical,

per se, that of a particle, where πD_p represents the circumference of the particle.

$$\alpha = \frac{\pi D_p}{\lambda} \tag{2.2}$$

By evaluating the non-dimensional parameter α, the influence of particle diameter can be used to identify three distinct modes of light scattering: Geometric, Rayleigh, and Mie. For large macroscopic particles, such as a glass marble, D_p is much larger than λ, therefore $\alpha \gg 1$. This is referred to as geometric scattering. At the molecular level, particle size is often smaller than λ; $\alpha \ll 1$, described as Rayleigh scattering. At the microscopic scale, D_p and λ are frequently close in value; therefore, α will approach unity. When $\alpha \approx 1$, the scatter is described as Mie scattering [11].

2.3.2 Measurement Process

PDPA systems utilize simultaneous observations of interferometric and light scattering processes to make useful measurements of physical phenomena. In order to make such observations, an array of optical devices must be integrated into components that, when assembled, form a functional system. With a familiarity of the fundamentals processes, the roles which these PDPA system components play in the measurement of particle velocity and diameter can now be elaborated upon. An illustration of PDPA components and basic system setup is featured in Figure 2.5.

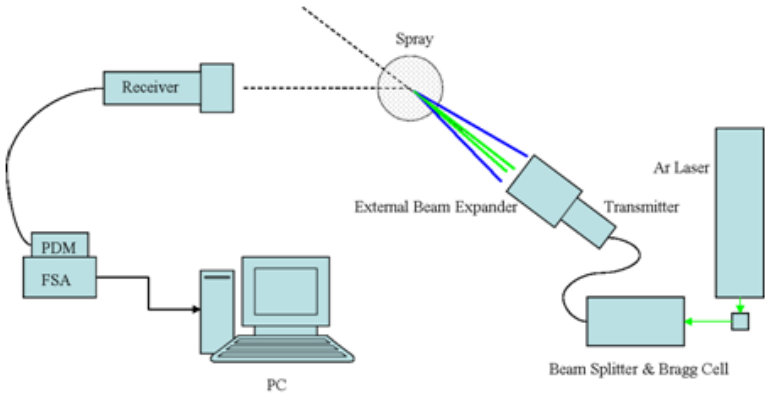

Figure 2.5: Phase Doppler Particle Analysis System Components

Laser light is supplied to the system from a parent beam generator. This single beam of collimated light is fed into an initial system component. Two types of optical devices within the first component perform critical operations on the parent beam: beamsplitters and Bragg cells. A series of beamsplitters separates the parent beam into three wavelength-distinct pairs of beams. A beamsplitter optic is typically composed of two quartz prisms, bonded together to form a cube. The thickness of the cube's adhesive layer is selected for a particular wavelength, and transmits half of the incident light- reflecting the other half. Next, a single beam from each pair is sent through a Bragg cell. Also known as an acousto-optic modulator, the Bragg cell consists of a Piezo-electric transducer which excites oscillation in a quartz optic. As it travels through the optic, the beam is diffracted. The phase of the diffracted beam is shifted by the phase of the sound waves.

Three beam pairs, each a distinct wavelength from one another, exit the initial PDPA component. Within each pair, a phase shift between each beam is present. Accounted for, a total of six beams are next transferred to the second component, the beam transmitter. The transmitter houses a variety of lenses and orientation devices to align the intersection of each beam pair at a precise point in space. The intersection of each beam pair — and resultant interference — produces a fringe pattern. Oriented in three different planes, the set of fringe patterns forms an integration region of space in which measurements can be made.

As a particle travels through the interrogation region's interference patterns, the beams are scattered. The manner in which the light is scattered is the crux of PDPA measurements. Due to the phase shift between the beams, each interference pattern consists of alternating constructive and destructive fringes. When a particle passes from bright fringe to dark fringe, "Doppler" bursts of both reflected and refracted light are generated. The increasing and decreasing intensity of a burst's waveform directly corresponds to the particle's movement through the fringes.

The light scatter information is gathered by the third major component of a PDPA system, the detector unit. Positioned at an angular offset from the interrogation region, the detector unit collects forward scattering information produced by the refraction of the fringes. The detector unit houses a variety of optics which, at three different positions, views specific wavelengths corresponding to a beam pair. The Doppler burst informa-

tion gathered by the detector is then transferred to an off-board Photo Detector Module (PDM).

Finally, a multi-bit digital processing unit, the FSA, applies signal processing techniques to the information gathered by the detector unit and PDM. The FSA performs a Fast Fourier Transform and autocorrelation of each signal to determine frequency and phase. These techniques, in conjunction with information known about the interference patterns of the probe volume, enable the measurement of velocity and diameter for each particle that travels through the interrogation region.

Since the applied phase shift between the transmitter's beams is precisely known, Equation 2.1 can be applied to determine the fringe spacing, Δ. With this known, the temporal frequency of the Doppler burst can be linearly related to particle velocity. Droplet diameter is determined by its linear proportionality to the phase shift of the Doppler burst.

CHAPTER 3

EXPERIMENTAL METHODS & INSTRUMENTATION

3.1 Injector Design

A common part, multi-configuration injector was designed to facilitate the study of LOX-LCH_4 performance in lunar ascent-class engines [12]. The Modular Injector for Scientific and Educational Research (MISER) was designed to operate in three separate modes to accommodate parametric studies for a variety of flow conditions. Based on full-scale engine operating conditions, designs for shear-coaxial, swirl coaxial, and dual-swirl injection schemes were integrated into a single, configurable device — easily modified to suit a desired experiment. The injector element was designed to operate at a nominal chamber pressure of 1.90 MPa (275 psig) and a total mass flow rate of 0.11 $\frac{kg}{s}$. Configured as a swirl coaxial injector element, the swirling central flow was designed for 0.082 $\frac{kg}{s}$ of LOX, and the exterior shear flow was designed to accommodate 0.028 $\frac{kg}{s}$ of LCH_4. Figure 3.1 illustrates a cross-sectional view of the MISER swirl coaxial injector element and manifold.

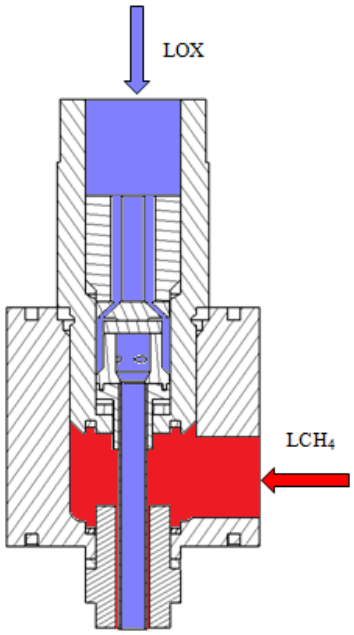

Figure 3.1: Cross-sectional View of MISER Injector Device with Flow Paths

The LOX post swirl element was designed in accordance with classic swirl injector design parameters and procedures outlined by Bazarov [13]. The element was designed to operate at 0.082 $\frac{kg}{s}$ mass flow, issuing a spray at a total angle of $90°$. A cross-sectional profile of the element geometry can be seen in Figure 3.2. Design parameters and physical dimensions of the swirl element are featured in Table 3.1.

Additionally, a scalability study was performed to investigate the implementation of H_2O as a simulant for LOX and the potential impact on the geometry of the injector design. Dimensional differences in the geometry designed for water, in comparison to the original LOX geometry, were identified to be within machining tolerances, therefore negligible. Acknowledging the inviscid nature of Bazarov's design theory, the conclu-

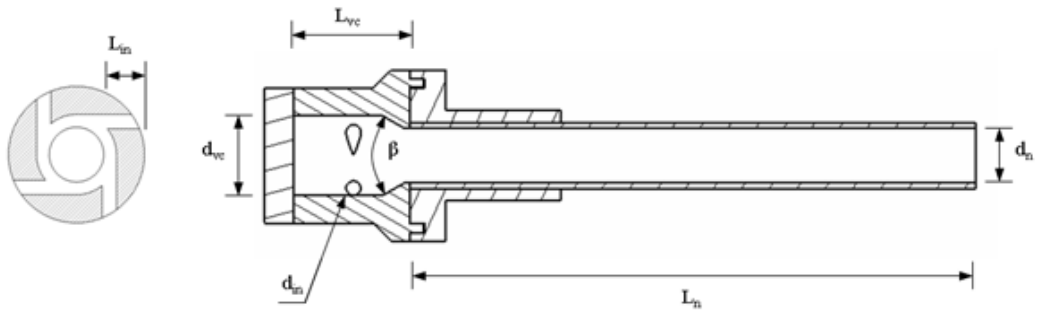

Figure 3.2: LOX Post Swirl Element Cross-section

Table 3.1: Dimensions and Design Parameters of the LOX Swirl Element

Design Parameter	Value
$\dot{m}$	0.082 $\frac{kg}{s}$
ΔP_{inj}	0.35 MPa
θ	90°
d_{in}	1.27 mm
L_{in}	2.53 mm
N	4
d_{vc}	7.00 mm
L_{vc}	3.20 mm
β	153°
d_n	5.00 mm
L_n	50.0 mm

sions of the scalability study were accredited to the comparable density of LOX to water.

The approach for this testing was to characterize the swirling spray of the MISER's interior LOX post, independent of the LCH_4 exterior shear flow. Although it was recognized that the inclusion of a liquid or gaseous exterior flow would drastically alter the spray characteristics of the injec-

tor, as a unit physics study of self-atomization, it was deemed valuable to exclusively assess the spray of the LOX swirl element.

3.2 Test Condition Analytics

A common merit of relative performance for sub-scale combustor testing is the efficiency of characteristic exhaust velocity. Equation 3.1 purely defines c^* as a function of chamber temperature and thermochemical gas properties: the ratio of specific heats (Γ), the universal gas constant (R_u), and molecular weight (MW).

$$c_t^* = \frac{\sqrt{\Gamma \frac{R_u}{MW} T_c}}{\Gamma \sqrt{\frac{2}{\Gamma+1}^{\frac{\Gamma+1}{\Gamma-1}}}} \tag{3.1}$$

In this form, c^* relates the energy release of the combustion reaction to the kinetic energy of the flow. It describes the theoretical energy limit of the combustion physics, and is independent from the geometric characteristics of the combustor [14].

To exploit this merit in a manner practical to sub-scale combustor testing, Equation 3.1 must be expressed in parameters that are easily determined, experimentally. Further manipulation of the isentropic rocket flow equations yields an expression of c^* in such terms, Equation 3.2. By normalizing a measured c^* by a theoretical value from Equation 3.1, a c^*-efficiency (η) is obtained as Equation 3.3.

$$c_e^* = \frac{P_c A_t}{\dot{m}_{total}} \tag{3.2}$$

$$\eta = \frac{c_e^*}{c_t^*} \tag{3.3}$$

Equation 3.2 highlights the direct relationship between characteristic exhaust velocity and chamber pressure. To this extent, a link between combustion and cold flow experiments can be established. Furthermore, with the implementation of Equation 3.4, chamber pressure conditions for cold flow experiments can be derived from η measurements of sub-scale combustion experiments.

$$P_c = \eta \left[\frac{\dot{m}_{total} \sqrt{\Gamma \frac{R_u}{MW} T_c}}{A_t \Gamma \sqrt{\frac{2}{\Gamma+1}^{\frac{\Gamma+1}{\Gamma-1}}}} \right] \tag{3.4}$$

Depending on the experimental setup of a uni-element combustion test, η can range in value from below 0.5 to well above 1.0; however, efficiencies above 100% are often a relic of sub-scale combustor heat transfer qualities. An injector flame can impinge on the chamber walls, whereby the chamber itself acts as a heat sink. This occurrence removes thermal energy from the combustion environment at an increased capacity, thus decreasing the heat release available for kinetic energy conversion.

Governed by Equation 3.4, as η decreases, chamber pressure shall decrease in proportion. Following suit, with a series of input η values and

Table 3.2: Chemical Equilibrium Properties for LOX-LCH_4 Combustion

Property	Value
$\dot{m}_{total}$	7.027 $\frac{kg}{s}$
P_c	1.90 MPa
ϕ	1.313
R_u	8314 $\frac{J}{kmol-k}$
T_c	3355 K
Γ	1.214
MW_{poc}	21.59 $\frac{kg}{kg-mol}$
A_t	$4.911x10^{-3}m^2$

pertinent gas properties, chamber pressure test conditions are calculated. Table 3.2 lists the gas properties of the LOX-LCH_4 products of combustion and nozzle geometric characteristics. These properties were generated by NASA's Chemical Equilibrium Analysis (CEA) code, based on input performance parameters stipulated by the lunar-ascent engine RFP.

Finally, with properties provided by the CEA analysis, Equation 3.4 can be evaluated with a set of input η values. Table 3.3 features cold flow chamber pressure conditions derived from expected c^*-efficiency values. Chamber pressure conditions are normalized to the nominal chamber pressure of 1.9 MPa.

Table 3.3: Chamber Pressure Conditions for Cold Flow Testing

η	0.38	0.50	0.65	0.76	0.87	1.1	1.4
P_c (MPa)	0.95	1.24	1.61	1.90	2.18	2.76	3.46
PR	0.50	0.65	0.85	1.00	1.15	1.45	1.82

3.3 Pressure Measurement Instrumentation

Although pressure measurements were gathered for monitoring purposes in numerous locations throughout the spray facility, specific locations were identified to be critical in collecting experimental measurements. To conduct such measurements, gage pressure transducers were installed. Details of the critical transducers are provided in Table 3.4. As one of the dependent variables of the experimentation, particular care was placed on the precise measurement of chamber pressure. Pressure measurements from the transducer upstream of the variable area cavitating venturi provided measurements for the control and calculation of liquid simulant mass flow rate, as will be discussed in 3.4.1. Additionally, as a means to confirm venturi cavitation and to measure ΔP across the injector, liquid simulant pressure measurements upstream of the injector were also of interest.

3.3.1 Transducer Calibration

Each transducer was subjected to calibration testing to determine an accurate correlation between output voltage and pressure — a correla-

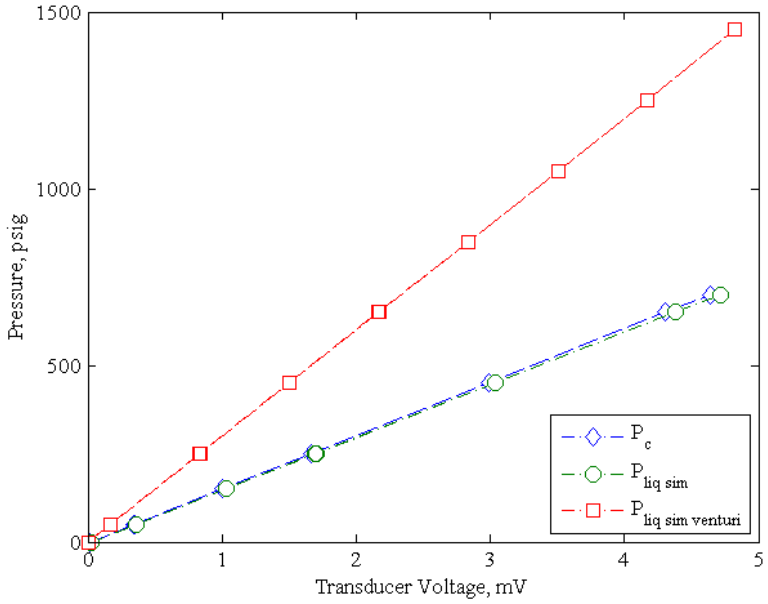

Figure 3.3: Pressure Transducer Calibration Data

tion unique to each device. A hydraulic dead-weight testing methodology was employed to gather linear calibration equations. Based on the fixed mass of the dead-weights, voltage output information was collected at several intervals across the entire range of each transducer. Figure 3.3 features calibration plots for the Chamber, Liquid Simulant Venturi, and Liquid Simulant Injection pressure transducers. Calibration equations are presented in Table 3.4.

3.3.2 Calibration Uncertainty Analysis

Close examination of the transducer calibration plots reveals important insight towards the very nature of calibration. Since the act of calibration is, in-and-of-itself, an experiment based on measured data, each

Table 3.4: Transducer Calibration Equations

Transducer	Range	Equation
Liquid Simulant Venturi	0-5 mV/0-1500 psig	$P = 300.1E - 1.226$
Liquid Simulant	0-5 mV/0-750 psig	$P = 149.1E - 3.458$
Chamber	0-5 mV/0-750 psig	$P = 151.3E - 2.201$

measurement will exert its own unique influence as a variable in the calibration equation. To identify the impact of each variable, it is pertinent to perform a regression analysis for the data set.

Calibration testing was performed through the spray facility's DAQ system as an effort to capture the systematic bias upon each transducer's measurements. Although random uncertainties can be identified for measurements made by each transducer on a test-to-test basis, an effort was made to identify the total uncertainty associated with each transducer's calibration — accounting for both random and systematic uncertainties.

As evidenced in the calibration plots, the linear pressure-voltage behavior of the transducers accommodates a regression model based on a least squares principle. Each calibration equation was applied as a data reduction equation in a Taylor Series propagation approach to uncertainty analysis, as per Coleman and Steele [15]. Equation 3.5 shows the generalized linear data reduction equation of the analysis.

$$P = q_{nom}E + c_{nom} \tag{3.5}$$

$$U_P = [s_P^2 + \sum_{i=1}^{n}(\frac{\partial P}{\partial P_i})^2 b_{P_i}^2 + 2\sum_{i=1}^{n-1}\sum_{k=i+1}^{n}\frac{\partial P}{\partial P_i}\frac{\partial P}{\partial P_k}b_{P_iP_k} + \sum_{i=1}^{n}(\frac{\partial P}{\partial E_i})^2 b_{E_i}^2 + 2\sum_{i=1}^{n-1}\sum_{k=i+1}^{n}\frac{\partial p}{\partial E_i}\frac{\partial P}{\partial E_k}b_{E_iE_k} + (\frac{\partial P}{\partial E_{new}})^2 b_{E_{new}}^2 + 2\sum_{i=1}^{n}\frac{\partial P}{\partial E_{new}}\frac{\partial P}{\partial E_i}b_{E_{new}E_i}]^{\frac{1}{2}} \tag{3.6}$$

Equation 3.6 represents the Taylor Series expansion of Equation 3.5, capturing the random and systematic influences of pressure and voltage in the uncertainty of the calibration. The s_P and b_{P_i} terms respectively represent the random and systematic uncertainties associated with the calibration's pressure measurements. The random uncertainty of pressure is defined as a function of the standard error of regression (SER), seen in Equations 3.7 and 3.8.

$$SER = \left[\frac{1}{n-2}\sum_{i=1}^{n}(P_i - q_{nom}E_i - c_{nom})^2\right]^{\frac{1}{2}} \tag{3.7}$$

$$s_P = SER\left[\frac{1}{n} + \frac{(E_{new} - \bar{E})^2}{\sum_{i=1}^{n}(E_i - \bar{E})^2}\right]^{\frac{1}{2}} \tag{3.8}$$

Systematic uncertainty of the pressure measurements introduced by the dead-weight calibration technique is captured as $b_{P_iP_k}$. Systematic uncertainties associated with voltage measurements are represented by b_{E_i} and $b_{E_iE_k}$. The systematic influence of perturbing voltage is shown as $b_{E_{new}}$ and $b_{E_{new}E_i}$.

Table 3.5: Expressions for Transducer Calibration Uncertainty

Transducer	Equation
Liquid Simulant Venturi	$U_P = 0.0294E^2 - 0.1300E + 0.636$
Liquid Simulant	$U_P = 0.0135E^2 - 0.0549E + 0.313$
Chamber	$U_P = 0.0122E^2 - 0.0485E + 0.275$

As an exercise in numerical methods, partial derivatives of pressure with respect to voltage measurements were approximated by Equation 3.9. To the same effect, Equation 3.10 approximates partial derivatives of pressure with respect to pressure measurements.

$$\frac{\partial P}{\partial E_i} \approx \frac{P_{pert,E_{new,i}} - P_{nom,E_{new,i}}}{.01E_{new,i}} \tag{3.9}$$

$$\frac{\partial P}{\partial P_i} \approx \frac{P_{pert,E_{new,i}} - P_{nom,E_{new,i}}}{.1} \tag{3.10}$$

Figure 3.4 features plots of total pressure uncertainty as a function of voltage for the Liquid Simulant Venturi, and Liquid Simulant Injection and Chamber transducers, respectively. Each figure illustrates uncertainty data with a superimposed fit, as well as the corresponding residual. Equations that describe the uncertainty curve-fits are presented in Table 3.5.

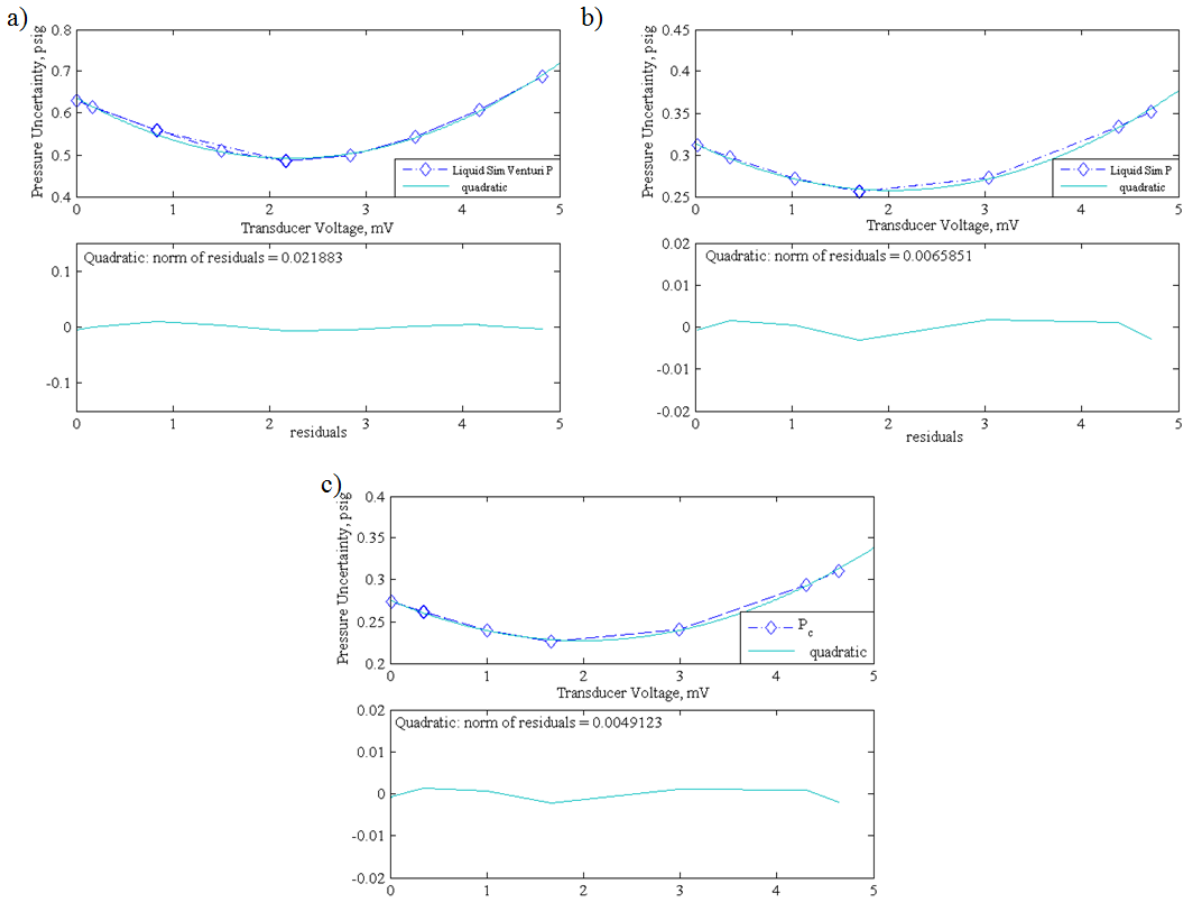

Figure 3.4: Uncertainty Associated with Pressure Calibrations: (a.) Liquid Simulant Venturi (b.) Liquid Simulant Injection (c.) Chamber

3.4 Variable-area Cavitating Venturi

To precisely control the metering of liquid simulant flow, a variable-area cavitating venturi was employed. The attractiveness of a cavitating venturi lies in its ability to maintain a desired flow rate - regardless of downstream pressure conditions. With a fixed upstream supply pressure, the flow rate through a cavitating venturi is independent of downstream pressure fluctuations. To ensure cavitation at the throat of the venturi,

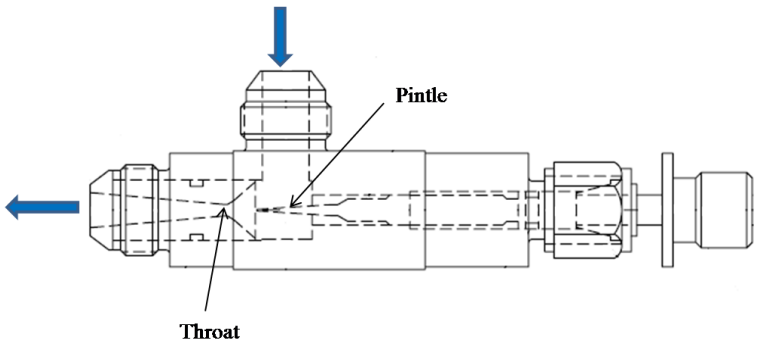

Figure 3.5: Profile of the Variable Area Cavitating Venturi

upstream pressure is typically maintained at $> 15\%$ of the maximum downstream pressure. The variable-area functionality of the venturi is a convenient feature that allows *in situ* adjustability of simulant flow rate. Figure 3.5 illustrates a cross section of the device. As the pintle is adjusted, the effective throat area changes.

An initial series of venturi calibration tests was performed. Due to the steady liquid simulant mass flow rate conditions of the experimentation, the variable-area function of the venturi was deemed unnecessary to the study. An alternative method of mass flow control with the device was pursued. Compared to a standard fixed-orifice, a venturi flow meter offers enhanced pressure recovery across the restriction: typically exceeding the 85^{th} percentile. In this regard, the use of a fixed-area venturi is often more beneficial than use of a standard orifice.

Using the initial calibration data as a guideline, a fixed pintle position, ergo fixed throat area, was sized to provide .082 $\frac{kg}{s}$ in consideration of two requirements. Firstly, in order to maintain cavitation, the $\Delta P_v > 15\%$

Table 3.6: Cavitating Venturi ΔP Conditions

PR	0.50	0.65	0.85	1.00	1.15	1.45	1.82
ΔP_v (%)	60	54	39	33	46	24	16

rule was to be conserved; secondly, downstream pressure was to be maintained at levels sufficient for injection over the entire range of chamber pressure conditions. To this extent, venturi operating conditions were interpolated; the venturi pintle length was set to 30.81 mm and pressure upstream of the venturi was maintained at 4.57 MPa. Pressure drop conditions across the venturi are shown in Table 3.6.

3.4.1 Mass Flow Rate Confirmation

Due to the unknown behavior of throat area with respect to pintle length, real-time calculation and monitoring of liquid simulant mass flow rate was called into question. To confirm the fidelity of mass flow rate to the operating conditions, direct measurements of $\dot{m}$ were gathered. After passing through the venturi, liquid simulant flow was diverted from the HiPSF to the ASF, granting physical access to the flow. An elementary, yet effective, method was developed to gather such measurements: a volume of simulant was collected and weighed, after which the mass of the simulant was divided by the interval of collection time. This method of mass flow confirmation was adopted as standard practice before each test.

3.4.2 Mass Flow Rate Uncertainty Analysis

Since direct measurement data of $\dot{m}$, via regular mass flow confirmation tests, was available, a Taylor Series expansion was applied to resolve uncertainties as a function of basic mass and time measurements, as described in Equation 3.11. The data reduction equation is simply $\dot{m} = \frac{m}{t}$; the associated partial derivatives are expressed in Equation 3.12 and Equation 3.13. The $\nu\sigma$ terms represent the random uncertainty based on a sample of size *n*.

$$U_{\dot{m}}^2 = (\frac{\partial \dot{m}}{\partial m})^2(\nu_n\sigma_m^2 + b_m^2)^2 + (\frac{\partial \dot{m}}{\partial t})^2(\nu_n\sigma_t^2 + b_t^2)^2 \tag{3.11}$$

$$\frac{\partial \dot{m}}{\partial m} = \frac{1}{t} \tag{3.12}$$

$$\frac{\partial \dot{m}}{\partial t} = \frac{-m}{t^2} \tag{3.13}$$

3.5 Imaging Studies

Backlit and stroboscopic visualization and imaging techniques were implemented to capture images of distinct spray features. A Nikon model D70 DSLR camera was remotely controlled by personal computer to take all images. Upon acquisition, images were initially post-processed through a gambit of software tools, including ImageJ, MATLAB, and MathCAD.

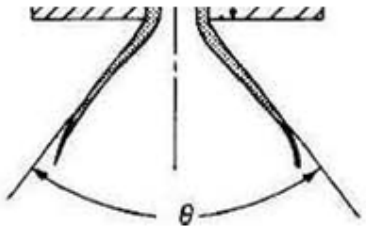

Figure 3.6: Schematic of the Free Cone Spray Angle [16]

Once post-processed, in-house codes were applied to analyze specific spray features. From such analyses, qualitative measurement of spray feature behavior was correlated to corresponding quantitative measurements of chamber pressure conditions.

3.5.1 Backlit Set-up & Methods

The free cone spray angle (θ), as characterized by Lefebvre [16], is seen in Figure 3.6. The θ is theoretically defined as the inverse tangent of the swirling sheet's tangential velocity-to-axial velocity ratio. To qualitatively measure the feature, backlit images of the spray were acquired. A backlit scheme was ideal for providing a clear contrast between the spray boundary and the surrounding environment.

For the backlit photography, a StockerYale model ML-0812 cold cathode fluorescent panel served as a uniform light source. Figure 3.7 illustrates the image acquisition system set-up for the backlit studies.

The Nikon D70 was outfitted with a Coastal Optics 105 mm lens. As to avoid a "freezing" effect of the conical sheet and droplets, a shut-

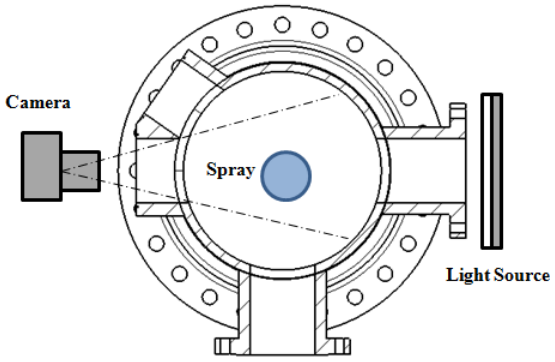

Figure 3.7: Experimental Set-up for the Backlit Imaging Studies

ter speed of 1.25 milliseconds and $f/4.5$ aperture were used to capture a uniform boundary. This practice served to effectively average the motion of the spray — temporally dampening the dynamics of the swirling sheet flow.

To examine the impact of chamber pressure on θ, a series of images was taken at each chamber pressure set point. First, chamber pressure conditions were brought to steady state. Triggering of the batch capture was then remotely issued. Simultaneous to the image capture trigger, pressure data were collected for each batch of images. Once images were acquired, chamber pressure was varied, and the data collection process was repeated. To ensure the scale of images from batch-to-batch and P_c-to-P_c was conserved, care was taken not to disturb the camera. A comparison of backlit images taken at each test condition can be seen in Figure 3.8.

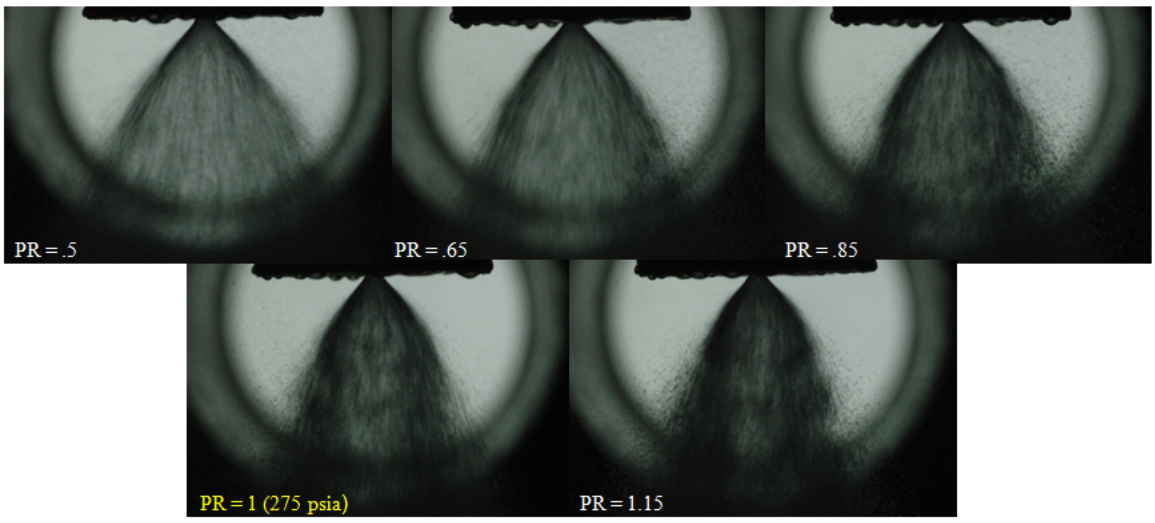

Figure 3.8: Backlit Images of the Spray as a Function of Chamber Pressure

3.5.2 Stroboscopic Set-up and Methods

Analogous to the intact core length observed in shear-coaxial injector sprays, the maximum axial distance from the injection plane at which the conical sheet remains intact is defined as the sheet penetration length (κ). The κ is a relic of atomization mechanisms, and the time scale magnitude of a fluid control volume's movement within the sheet is small. Although mechanical shutter speeds can operate on such time scales, it can be difficult to obtain light levels of sufficient intensity. This often leads to a loss in overall image detail due to a reduced depth-of-field.

For the stroboscopic imaging, a Shimpo Instruments model DT-311A xenon stroboscope was employed as the light source. Positioned normally to the camera's line-of-sight, the strobe functioned as a back light for the spray. Oriented in this manner, the intensity of the xenon

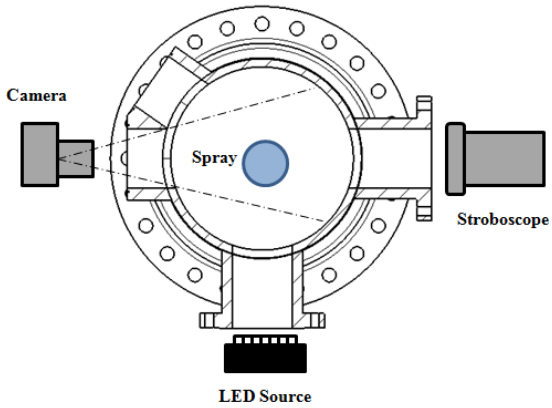

Figure 3.9: Stoboscopic Imaging Set-up

burst increased the captured detail of the spray's forward-scattered light. Additionally, a non-uniform LED light source was used to increase the amount of available ambient light within the chamber. Figure 3.9 is a schematic of the stroboscopic imaging set-up.

A Nikon model AF Micro Nikkor 105 mm lens was mounted to the D70 camera. As outlined in Section 2.2.2, a strobe of 5.47 Hz was used in conjunction with a camera shutter speed of 2 milliseconds and an $f/4$ aperture. The stroboscopic effect served to artificially augment the shutter speed of the camera. The increased temporal resolution provided by the strobe permitted the imaging of a distinct conical sheet and droplets. As outlined in the previous section, the exact experimental procedures employed in backlit imaging were applied to the acquisition of the stroboscopic images. Figure 3.10 features a comparison of stroboscopic images over the test conditions.

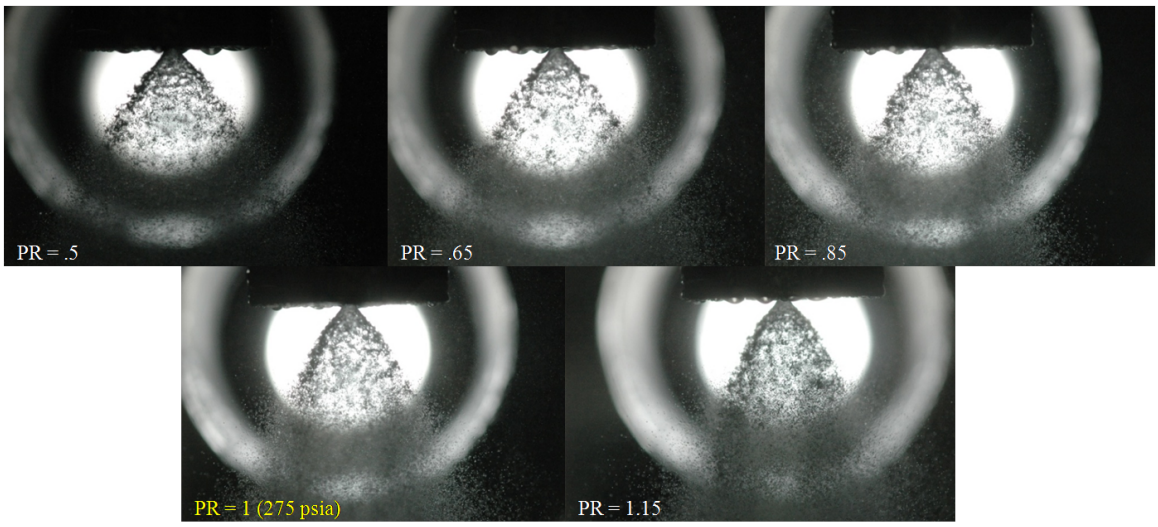

Figure 3.10: Stroboscopic Images of the Spray as a Function of Chamber Pressure

3.6 PDPA Studies

Central to this study, PDPA experiments were conducted to quantify self-atomization characteristics of the spray. A two-dimensional PDPA system was utilized to acquire flow properties of discrete droplets issued from the swirling, conical sheet. The system enabled the measurement of droplet velocities in the axial and radial directions. Corresponding droplet diameters measurements were also gathered by the system; of interest were mean diameter and Sauter mean diameter. Mean diameter represents the statistical mean of all particles that travel through the probe volume, and reflects the raw diameters of the processed bursts. Defined in Equation 3.14, Sauter mean diameter is also a statistical mean of all particles that travel through the probe volume; however, it also provides an additional

gage of droplet volume and surface area. An in-depth review of diameter nomenclature is provided by Sirignano [17].

$$d_{32} = \frac{d^3}{d^2} = 6\frac{\forall}{A} \tag{3.14}$$

Droplet properties were gathered within the spray's region of initial breakup- the primary atomization zone as discussed by Hulka and Makel [18]. As a strong function of κ for swirl injectors, and ***vis-á-vis*** of chamber pressure, the location of the primary atomization zone was identified by the scrutinization of stroboscopic images at each test condition. To this extent, the information from the sheet penetration length study proved invaluable in guiding the selection of PDPA measurement locations.

To determine the validity of measurements, the PDPA software applies a spherical criterion to the geometry of each droplet that passes through the probe volume. With such a criterion in consideration, if it is desired to gather measurements within the primary atomization regime, the probe must be isolated from the non-spherical ligaments and membranes associated with the initial breakup of the swirling sheet. Therefore, probe volumes for all tests were located 1 mm below the κ - assuring an axial plane on which valid droplet measurements within the primary atomization zone could be gathered. An example of the targeted PDPA measurement region is illustrated in Figure 3.11 and demarcates the pri-

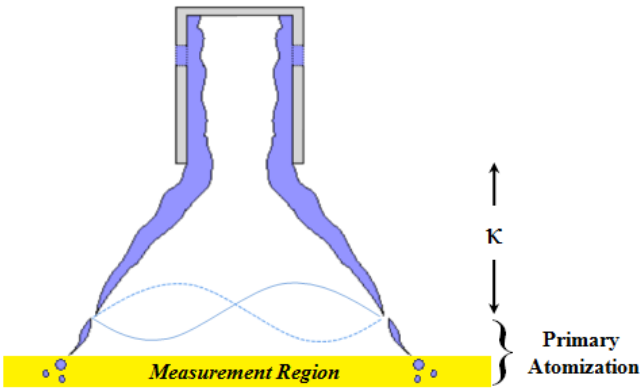

Figure 3.11: Targeted PDPA Measurement Region within the Primary Atomization Zone

mary atomization zone. Additional measurements were gathered on a reference plane several nozzle diameters downstream of the primary atomization zone. Held constant, measurements along the reference plane served as a baseline between test conditions.

An effort was made to spatially map droplet properties in a sweep across the spray diameter, along the primary atomization plane. Since the PDPA interrogation region was a fixed point in space, the spray, itself, was translated relative to the interrogation region. Assuming a quasi-axisymmetric spray morphology, to begin, the spray cone was centered on the PDPA beam crossings, in the axial measurement plane. As per indication from the stroboscopic images, the injector manifold was translated radially so to position the probe at the edge of the spray cone — near the bulk flow of droplets. Next, the injector manifold was translated in a fashion to sweep the probe volume across the entire spray envelope, whereby

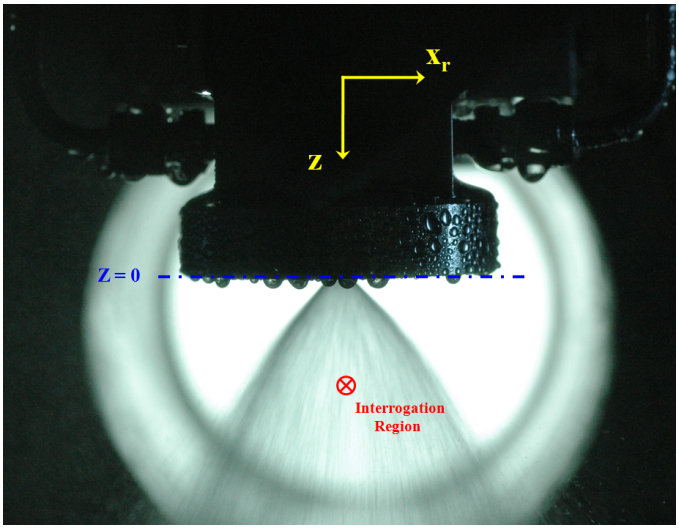

Figure 3.12: Coordinate System of Spray Translation

droplet measurements were collected in consistent spatial increments. The translational coordinate system is seen in Figure 3.12.

To provide a baseline spatial reference point valuable to future CFD efforts, an additional axial plane on which PDPA measurements were to be collected was chosen. The reference plane was common to all test conditions, and was selected to link data from the pressurized studies with data from previous studies performed at ambient atmospheric pressure [19]. From the atmospheric data, the plane within the primary atomization region was chosen to serve as the reference plane at pressurized conditions.

For each PR test condition, chamber pressure was brought to a steady state condition. Simultaneous to the triggering of PDPA measurements, pressure data were gathered. Measurements of chamber and liquid simulant pressure were collected over the sampling time of each PDPA run

in an effort to correspond with velocity and diameter measurements. Upon run data acquisition, the injector manifold was translated, and acquisition was repeated.

3.6.1 Set-up

A schematic of the PDPA set-up is illustrated in Figure 3.13. An Aerometrics FiberLight unit was supplied laser light from a Lexel model 95, 8 W capacity generator. The beam splitters and Bragg cell within the FiberLight unit respectively separated the parent beam into four lasers, phase-shifting two. The lasers were then fed to a TSI model 450410 transmitter and TSI model XPD50-E external beam expander. The receiver, TSI model 450305, gathered light scatter signals 35° off-axis to the transmitter. Signals were collected by the TSI PDM 1000 photo detector module, whereby they were processed by the TSI FSA 4000 unit. Finally, data were processed via FlowSizer software on board the system computer. Table 3.7 lists specific PDPA parameters and settings used during the experimentation.

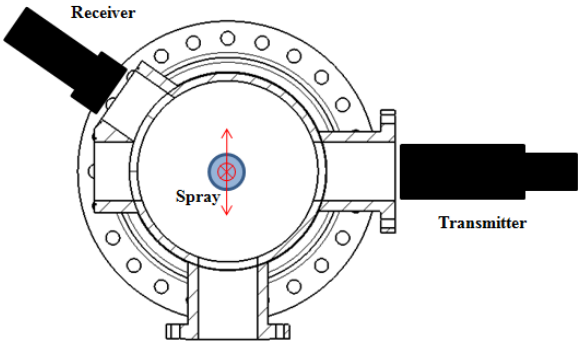

Figure 3.13: PDPA Experimental Set-up with Spray Translation Directions

Table 3.7: Optical Settings for PDPA

Parameter	Value
Transmitter L_f	750 mm
Receiver L_f	500 mm
Slit Aperture	150 μm
Parent Beam Power	400 mW
514.5 nm Beam Power	28 mW
488 nm Beam Power	9 mW
Beam Waist ch_1,ch_2	131.55, 124.78 μm
Max Velocity Limit ch_1,ch_2	36.59, 34.71 $\frac{m}{s}$
Min/Max Diameter	0.80/314.29 μm

CHAPTER 4

ANALYSIS & RESULTS

4.1 Spray Angle Measurements

An objective image analysis process was developed to measure θ for each test condition. Firstly, each individual image was converted from 8-bit RGB to grayscale. Next, the pixel intensities for each image were averaged together across an entire batch. The batch averaging produced a single mean image for the batch. Finally, the single averaged image was processed through a spray angle analysis code.

Employing an initial variety of image processing subroutines, the spray angle analysis code detects the liquid-to-gas boundary of the swirling sheet. Figure 4.1 is an example of a processed image overlaid with edges detected by the code. Once both left-side and right-side spray edges are detected and defined, the slope of each edge is calculated. Next, the angle of the edges is calculated from by the arctangent of the inverse slopes. Finally, the total free cone spray angle is computed by the addition of the two edge angles.

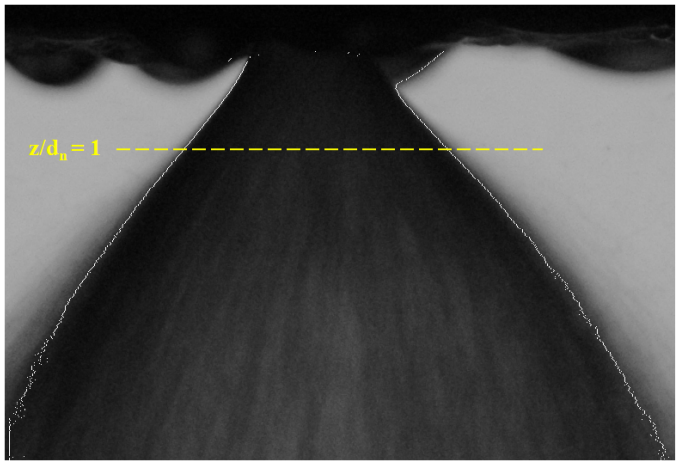

Figure 4.1: Detected Spray Boundaries Superimposed on a Processed Backlit Image

Table 4.1: Measurements of θ with Variation in Chamber Pressure

PR	0.50	0.65	0.85	1.00	1.15	1.45	1.82
Subjective θ (°)	82.22	80.31	81.40	80.02	79.07	79.52	77.70
Objective θ (°)	83.34	83.25	83.15	83.39	81.68	80.26	78.85

Measurements output from the spray angle analysis code were plotted as a function of *PR* to conclude the analysis; such measurements can be found in Table 4.1. Figure 4.2 illustrates the influence of chamber pressure conditions on θ, highlighting results from both subjective and objective analyses and compared with swirl injector design theory. Objective measurements were collected at 1 normalized nozzle diameter downstream of the injection plane. Uncertainty associated with both chamber pressure and mass flow rate measurements was on the order of 1% at 95% confidence.

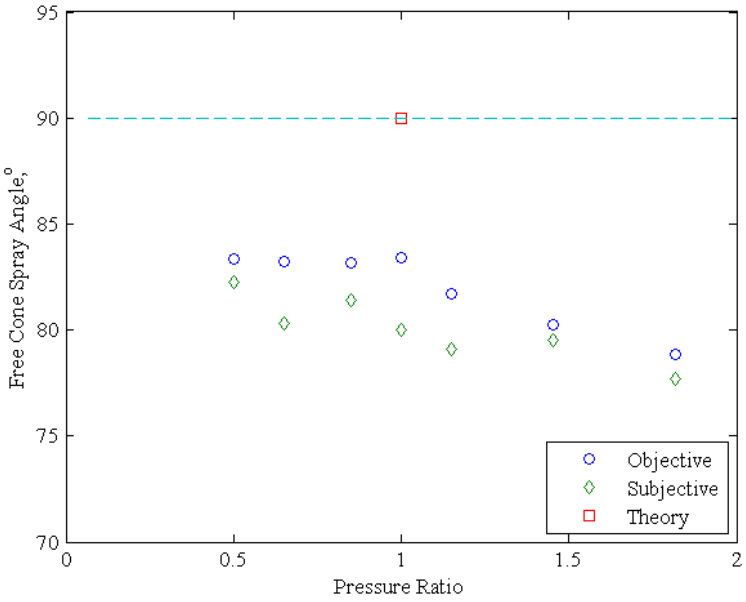

Figure 4.2: Free Cone Spray Angle with Variation of Steady Chamber Pressure

4.2 Sheet Penetration Length Measurements

Image processing techniques allowed for the qualitative measurement of κ. In a consistent fashion, sheet penetration length was identified for each image within an operating condition batch. A statistical mean of κ for a batch was then calculated, yielding an average measurement of κ at a given chamber pressure.

The sheet penetration length can be thought of as the axial plane at which aerodynamic forces become the dominate flow mechanism over the sheet's centrifugal momentum, breaking the sheet into ligaments and discrete droplets. To compare κ over chamber pressure conditions, it was deemed appropriate to identify the liquid sheet's aerodynamic *We* for

each test condition. Defined in Equation 4.1, the aerodynamic ***We*** is the traditional definition of ***We*** then normalized by the gas-to-liquid density ratio.

$$We_a = \frac{\rho_g}{\rho_l} We = \frac{\rho_g \rho_l u^2 h}{\rho_l \gamma} = \frac{\rho_g u^2 h}{\gamma} \tag{4.1}$$

A proposed empirical relation by Suyari and Lefebvre [20] was invoked to determine the sheet thickness at the injection plane (h) as a means to calculate We_a. Sheet thickness at the injection plane is defined by Equation 4.2 as

$$h = 2.7 \left[\frac{d_n \dot{m} \mu}{\rho_l \Delta P_{inj}} \right]^{.25}. \tag{4.2}$$

In the relation, d_n is the nozzle diameter, μ is the liquid dynamic viscosity, and ΔP_{inj} is the measured pressure drop across the injector. An expression of mass flow rate applied to the injector geometry, Equation 4.3, was used to calculate u, the axial velocity at the nozzle exit.

$$u = \frac{\dot{m}}{\rho_l \pi h (d_n - h)} \tag{4.3}$$

The influence of chamber pressure on κ is illustrated in Figure 4.3. Furthermore, the plot featured in Figure 4.4 highlights the aerodynamic effects of chamber pressure increase imparted on κ. Values featured in

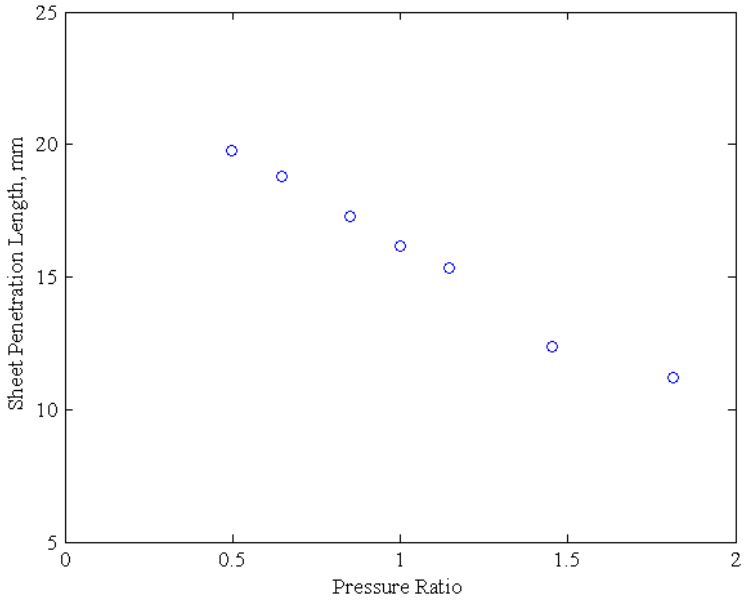

Figure 4.3: Sheet Penetration Length as a Function of Chamber Pressure

Table 4.2: κ Measurements and We_a with Variation in Chamber Pressure

PR	0.50	0.65	0.85	1.00	1.15	1.45	1.82
κ (mm)	19.8	18.8	17.3	16.2	15.6	12.4	11.2
We_a	140	182	238	280	323	399	464

Figure 4.4 are reflected in Table 4.2. The uncertainty of chamber pressure and mass flow rate was 1% on a 95% confidence interval.

4.3 PDPA Measurements

4.3.1 Atmospheric Experiments

As a baseline study, an initial series of experiments was conducted on the test article at atmospheric back pressure [19]. PDPA measure-

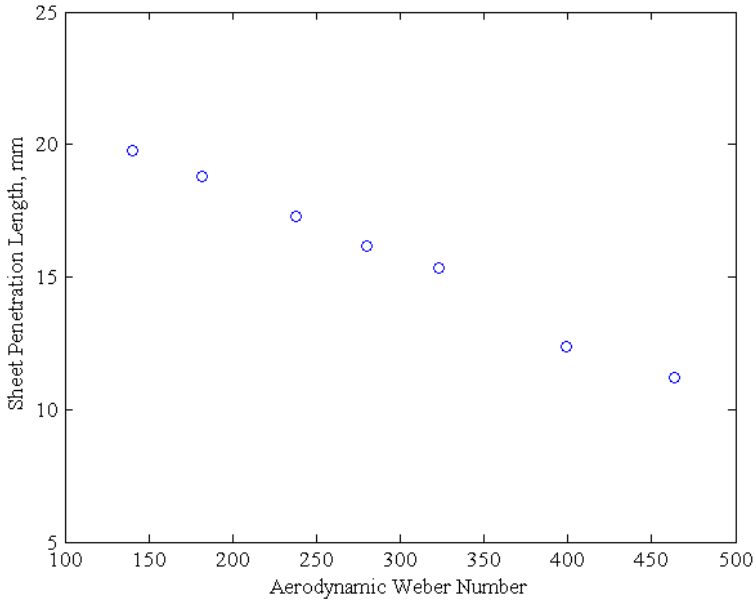

Figure 4.4: The Influence of Aerodynamics Imposed on the Liquid Sheet

ments were made within the spray's primary atomization region, in a sweep across the diameter of the spray envelope — spatially mapping mean axial velocity (V_a) and d_{32} of droplets. Figure 4.5 features a plot of mean axial velocity as a function of radial position. Figure 4.6 charts d_{32} as a function of radial position. The axial position within the primary atomization region is of particular importance; this position was used as the reference plane for measurements collected at pressurized experiments.

4.3.2 Pressurized Experiments

Following the experimentation strategy outlined in Section 4.3.1, PDPA measurements were gathered in the pressurized environment of the HiPSF spray chamber. Mean axial and radial components of droplet

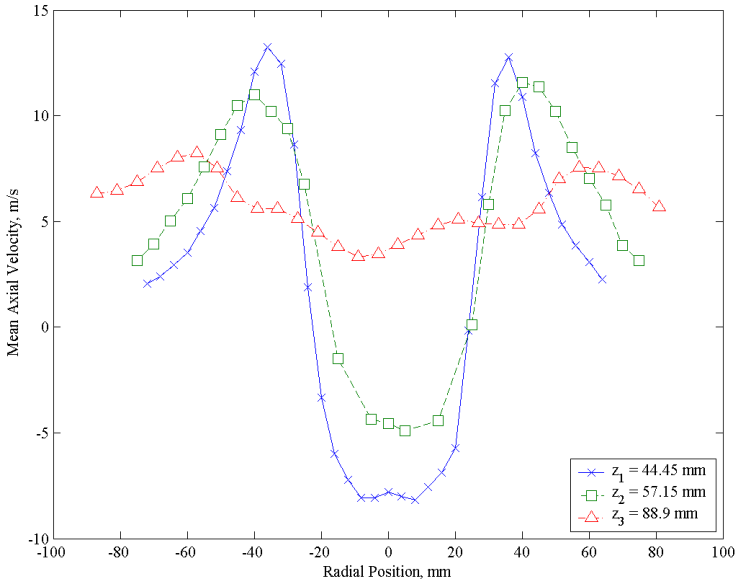

Figure 4.5: Droplet Mean Axial Velocities within the Primary Atomization Zone at Atmospheric Back Pressure

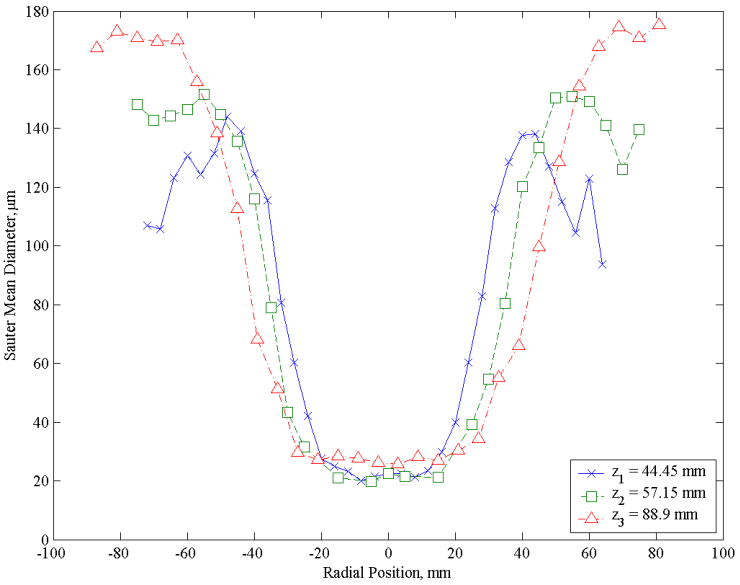

Figure 4.6: Droplet Sauter Mean Diameters within the Primary Atomization Zone at Atmospheric Back Pressure

velocity were measured over all test conditions. Additionally, droplet diameter statistics and distributions were gathered.

In order to shed light on droplet behavior with respect to chamber pressure, droplet data were processed and analyzed in a variety of manners. Firstly, to understand the physical trends of droplet velocities and diameters with respect to space for a given test condition, it was useful to first view such measurement sets individually. Figure 4.7, Figure 4.8, Figure 4.9, Figure 4.10 each represent spatial profiles of V_a, mean radial velocity (V_r), d_{10}, and d_{32}, respectively, for the nominal *PR*. At 95% confidence, the uncertainty associated with chamber pressure and mass flow measurements was found to be on the order of 1% and 0.5%, respectfully. Each plot reflects measurements collected in both the primary atomization zone and at the reference plane. Similar plots for the other *PR* conditions are found in Appendix B.

An additional analysis tool was developed to condense this data in a meaningful way. Vector-bubble plots of V_a and d_{32}, respectively, were superimposed to yield a useful qualitative view of droplet behavior in the flow field. The magnitude of each vector and arrow head corresponds to velocity magnitude in the axial direction, while bubble diameter corresponds to d_{32}. Figure 4.11 features a plot at the nominal *PR* condition. Additionally, plots for all remaining test conditions can be seen in Appendix C.

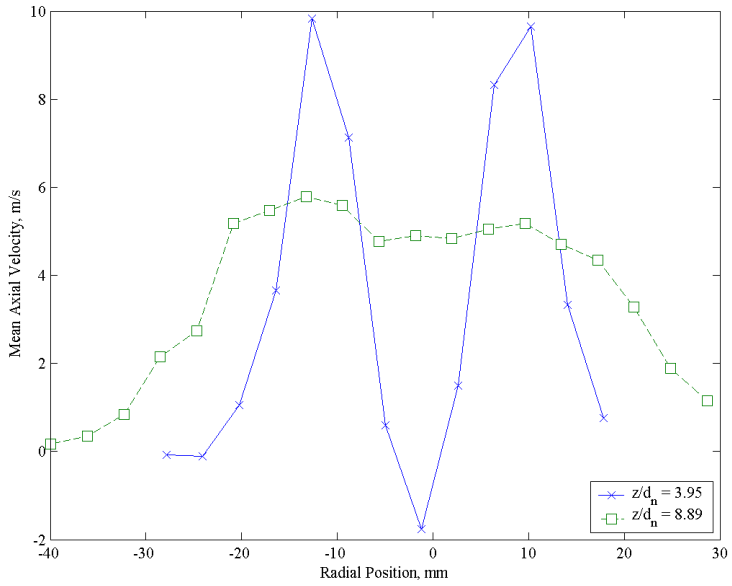

Figure 4.7: Mapping of Droplet Mean Axial Velocity at $PR = 1$

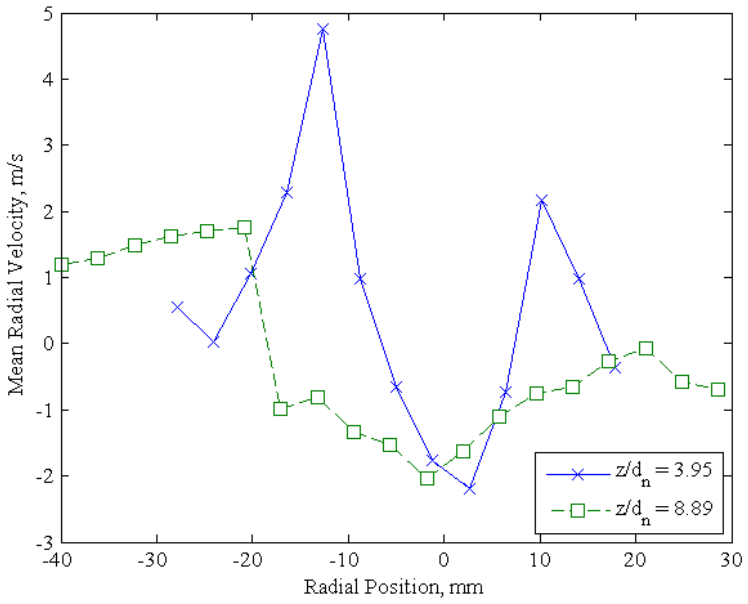

Figure 4.8: Mapping of Droplet Mean Radial Velocity at $PR = 1$

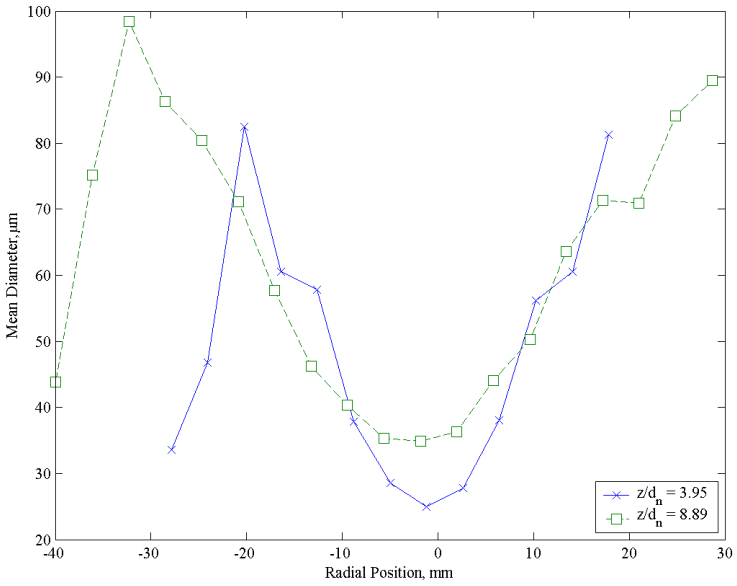

Figure 4.9: Mapping of Droplet Mean Diameter at $PR = 1$

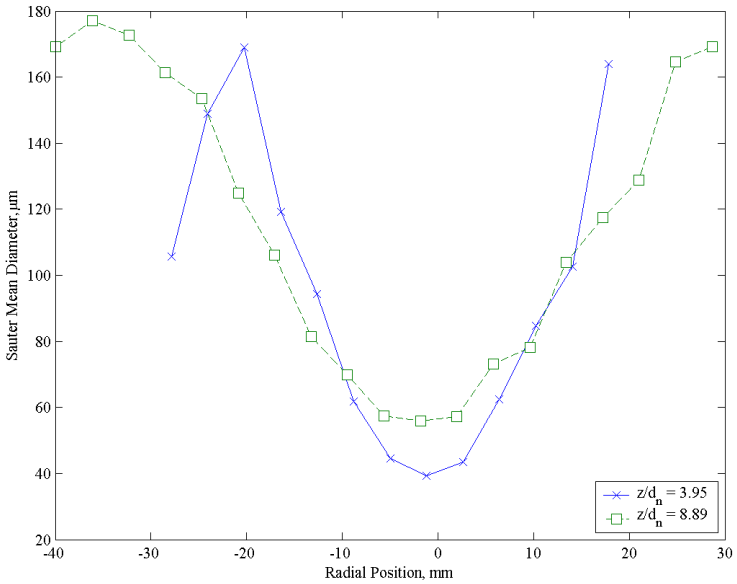

Figure 4.10: Mapping of Droplet Sauter Mean Diameter at $PR = 1$

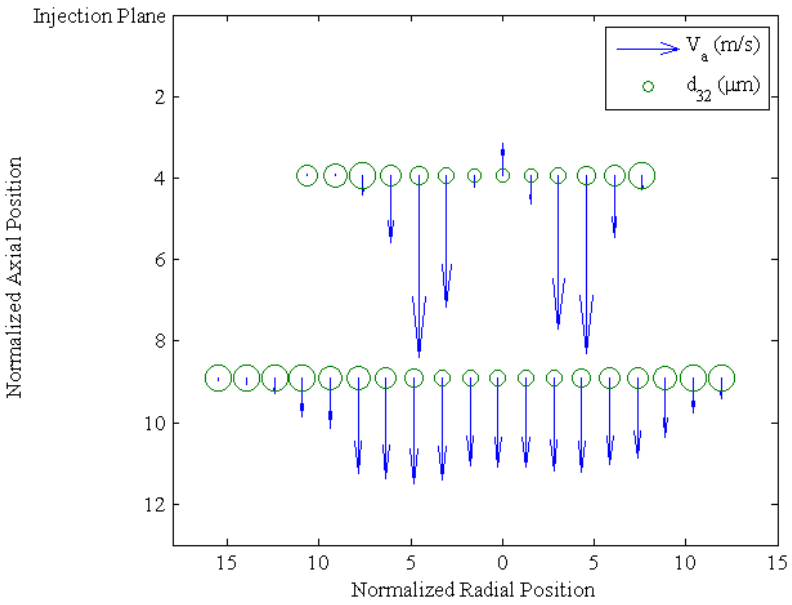

Figure 4.11: Axial Flow Field and Diameters of Droplets at $PR = 1$, x_r normalized by $\frac{d_n}{2}$

Droplet diameter distributions were also processed on a *PR* condition-by-condition basis. Spatial mapping of mean diameter distributions were plotted within the primary atomization zone. At the nominal *PR* condition, Figure 4.12 illustrates the statistical distribution profiles of d_{10} for each discrete measurement point across the diameter of the spray. Distribution maps for the additional chamber pressure conditions are located in Appendix D.

The next analytical step was to process the data in a manner in which the effect of chamber pressure on the spatial profiles of droplet behavior could be discerned. To gain the desired perspective, a profile for each droplet property, at each *PR* condition, was plotted. Figure 4.13

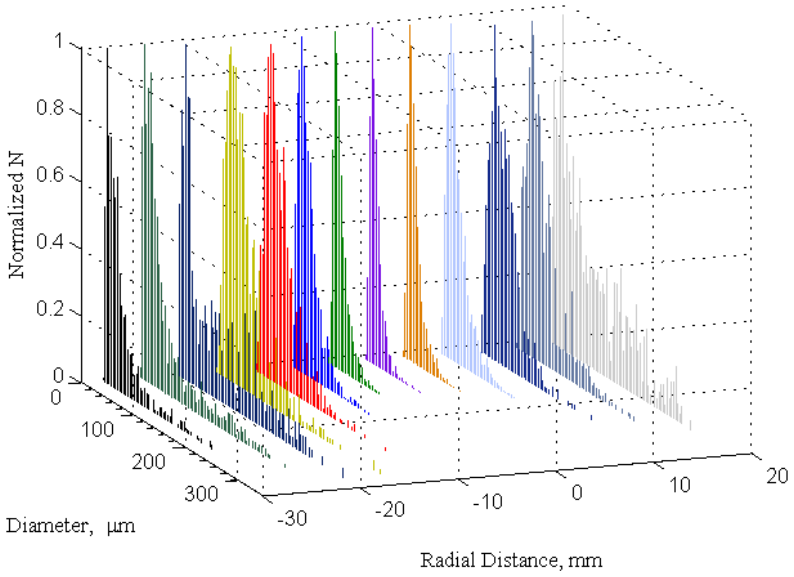

Figure 4.12: Diameter Distribution Profile Mapping at $PR = 1$

through Figure 4.16 plot multiple spatial profiles of V_a, V_r, d_{10}, and d_{32}, respectively — spanning the range of test *PR* conditions. These figures reflect measurements within the primary atomization zone, and include values measured at *PR* condition of 1.82, but excluding *PR* = 1.45. Plots corresponding to measurements collected on the reference plane can be found in Appendix E, but do not include the additional *PR* condition.

Prominently illustrated in Figure 4.13 and Figure 4.15, the measurement of negative velocities and diminished droplet diameters near the center of the spray appears to be a key indication of a known swirl injection behavior. The issued conical sheet of the spray encloses a region of circulating gas, stimulated by the swirling motion of the sheet. The vortex nature of the region is represented in Figure 4.17.

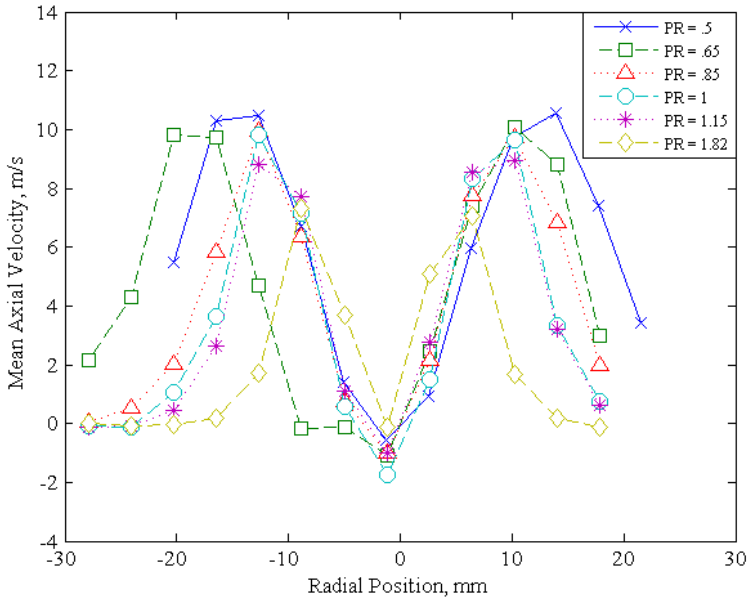

Figure 4.13: Comparison of Mean Axial Velocity Profiles in the Primary Atomization Zone

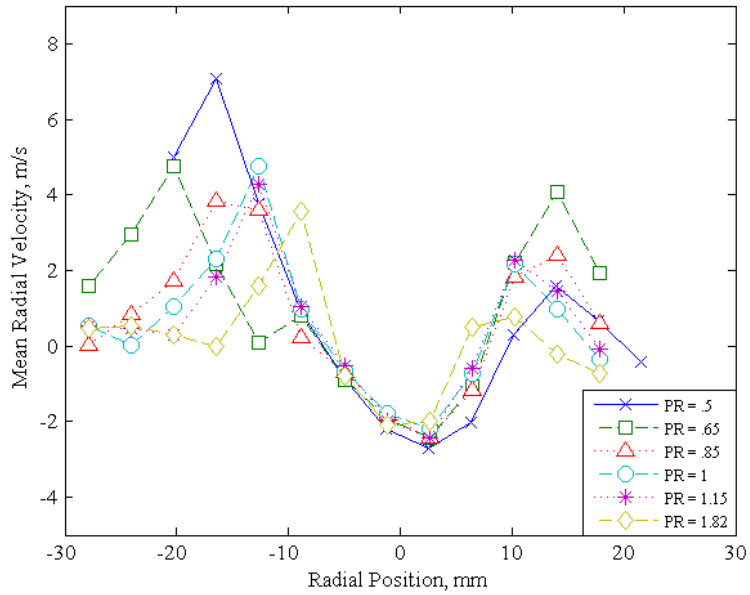

Figure 4.14: Comparison of Mean Radial Velocity Profiles in the Primary Atomization Zone

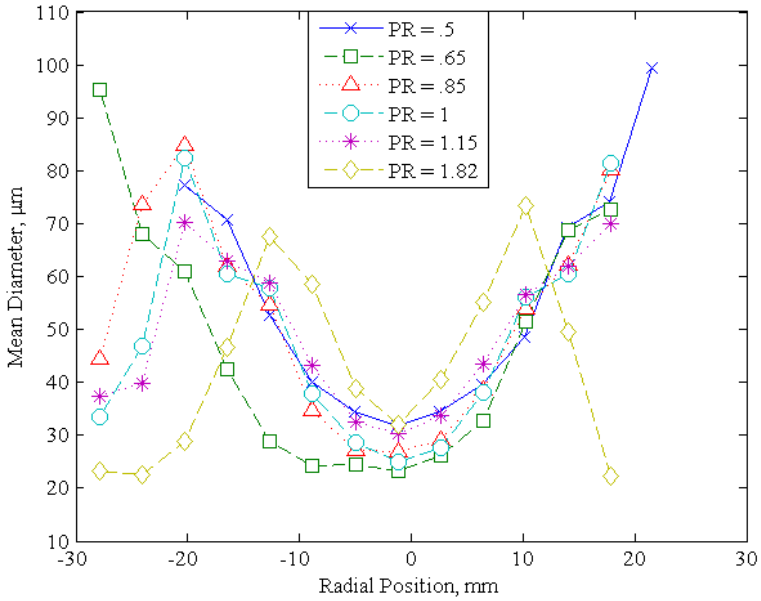

Figure 4.15: Comparison of Mean Diameter Profiles in the Primary Atomization Zone

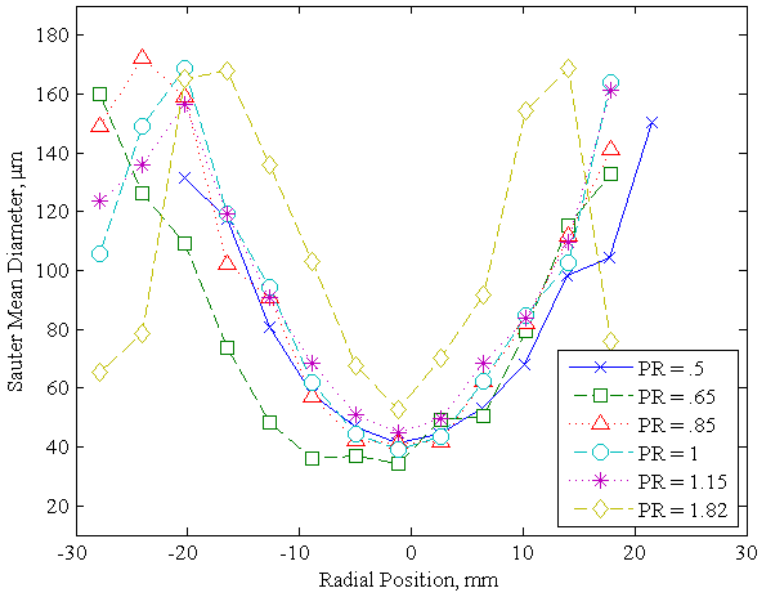

Figure 4.16: Comparison of Sauter Mean Diameter Profiles in the Primary Atomization Zone

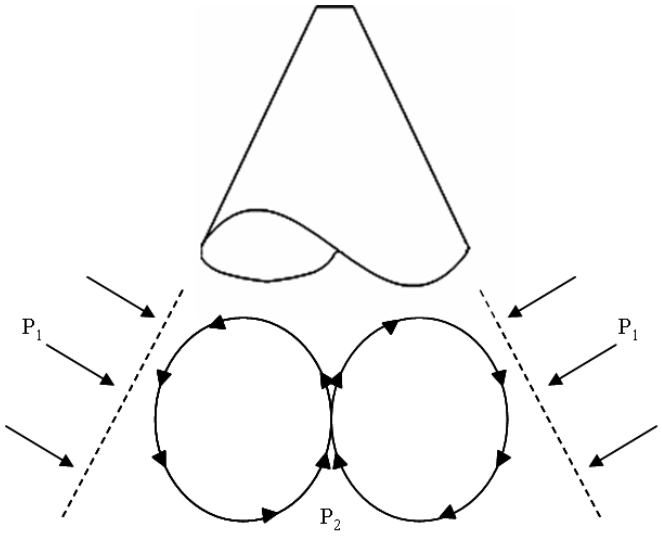

Figure 4.17: Recirculation Region Within the Hollow Spray Cone, where $P_2 < P_1$

To further highlight the effects of *PR* on the spatial profiles of V_a and d_{32}, data from the atmospheric back pressure study was included in the analysis. Figure 4.18 and Figure 4.19 are supplemented with atmospheric data, as seen in Figure 4.5 and Figure 4.6, collected in the primary atomization zone.

To fully assess the influence of chamber pressure on self-atomization, it becomes important to identify the *bulk flow* of droplets in the primary atomization zone. Firstly, it is assumed that a high number of droplets are measured within the region of space in which the bulk flow travels through. This assumption is reflected in a large distribution width on the diameter distribution plots. Secondly, droplets in the bulk flow are assumed to have the highest momentum in the flow field, therefore having the highest velocity and/or largest mass (manifested in volume as d_{32}) in the flow

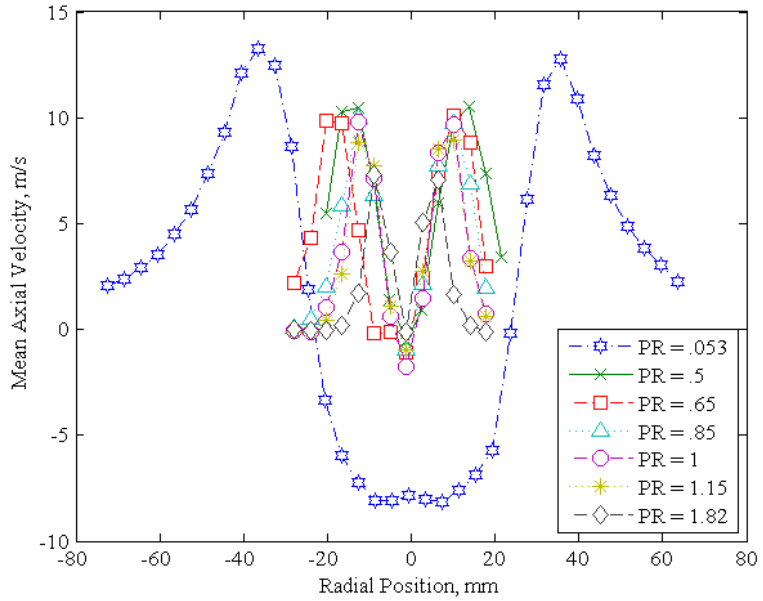

Figure 4.18: Comparison of Mean Axial Velocity Profiles in the Primary Atomization Zone — Including Atmospheric Pressure

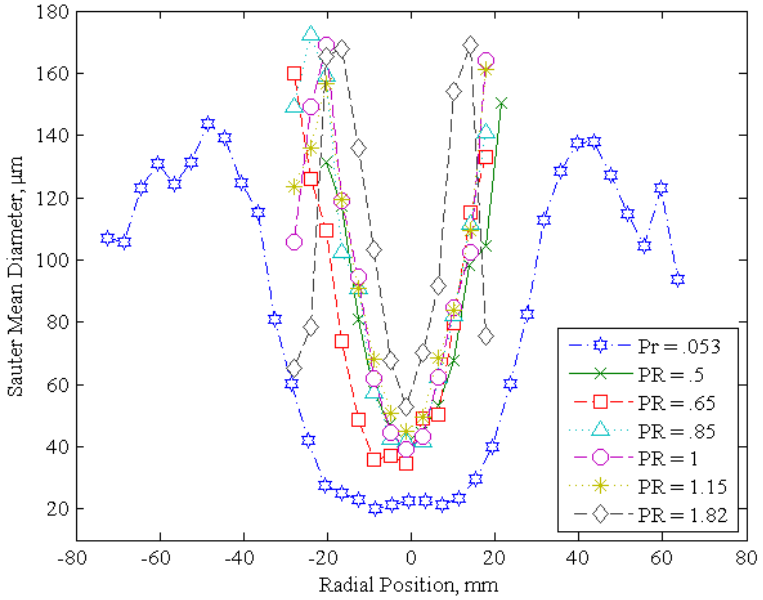

Figure 4.19: Comparison of Sauter Mean Diameter Profiles in the Primary Atomization Zone — Including Atmospheric Pressure

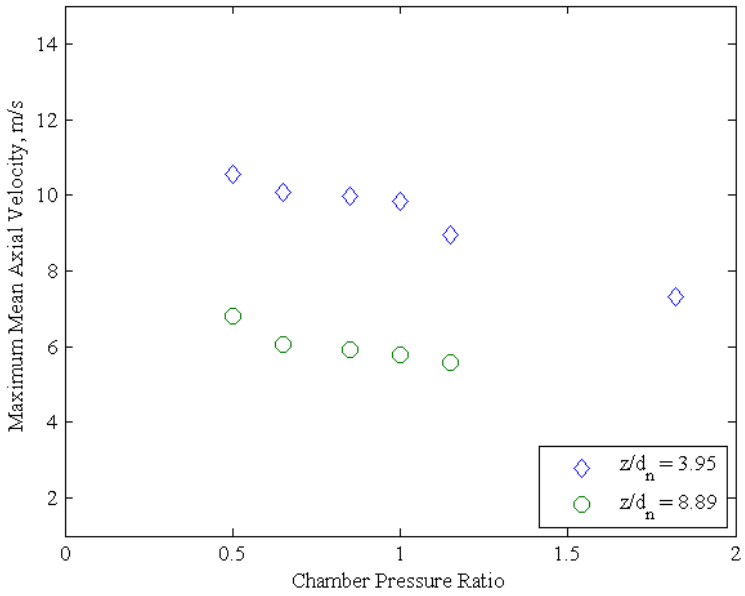

Figure 4.20: The Influence of Chamber Pressure on Droplet Mean Axial Velocity

field. This assumption is observed in the qualitative vector-bubble plots as the largest magnitude vector and/or bubble diameter. Additionally, the assumption is reflected in the *PR* comparison plots as the peak value on each profile.

With these criteria satisfied, maximum values can be parsed from each data set. These maximum values are indicative of the bulk flow, and can be compared over the test *PR* conditions in order to assess the effects of chamber pressure. This analysis technique finally yields an observation of self-atomization as a function of *PR*. The influence of chamber pressure on V_a, V_r, d_{10}, and d_{32} are illustrated in Figure 4.20 through Figure 4.23, respectively.

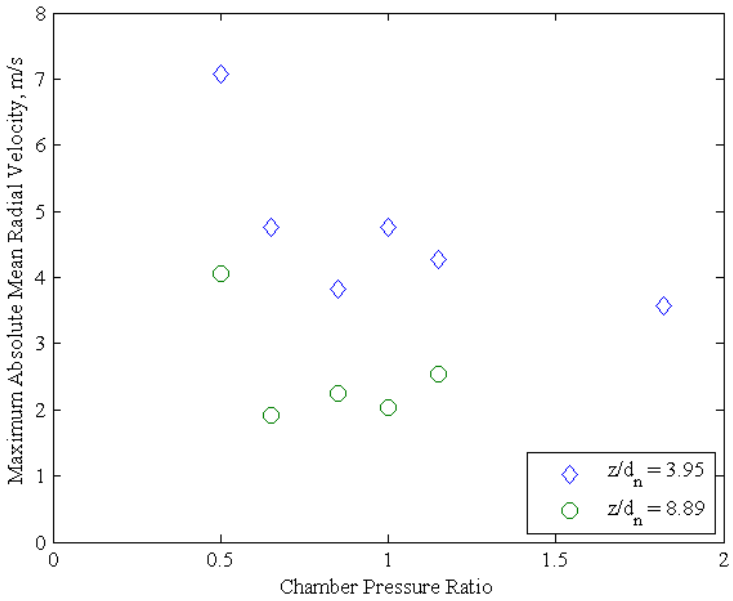

Figure 4.21: The Influence of Chamber Pressure on Droplet Mean Radial Velocity

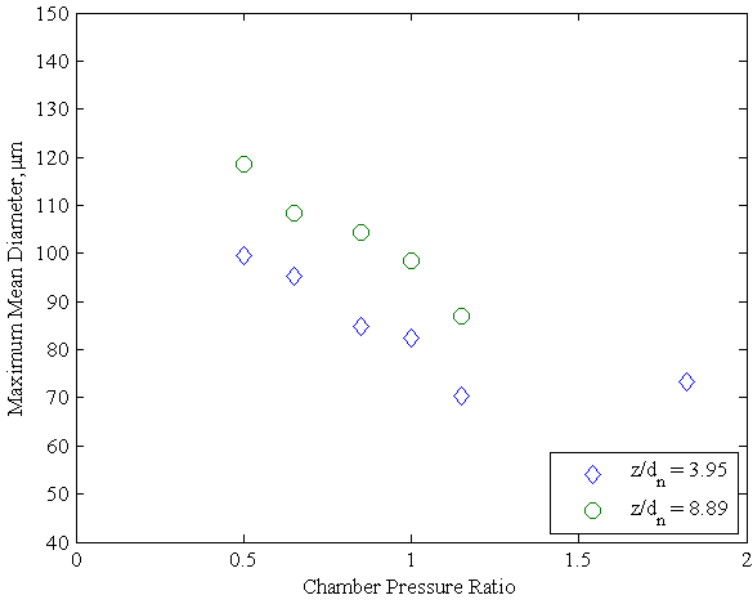

Figure 4.22: The Influence of Chamber Pressure on Droplet Mean Diameter

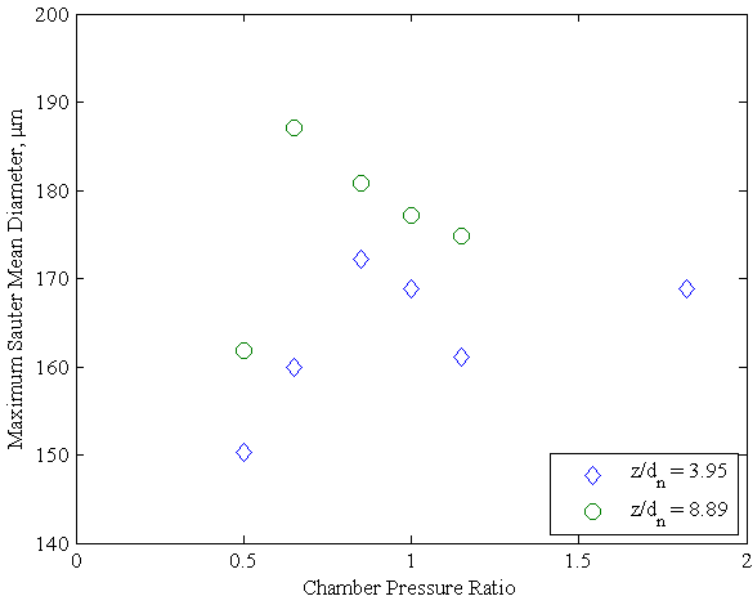

Figure 4.23: The Influence of Chamber Pressure on Droplet Sauter Mean Diameter

CHAPTER 5

DISCUSSION

5.1 Spray Structure Studies

Qualitatively, backlit image comparison revealed a distinct change in spray morphology as chamber pressure conditions increased. As a result of an objective image analysis methodology, the free cone spray angle was found to decrease with a positive variation in chamber pressure — seen in Figure 4.2. As suggested by Kenny [5], free cone spray angle is highly dependent on the film thickness (h) at the point of injection. Gas density increases as the chamber pressure increases; Kenny observed a discrepancy between the density of the quiescent environment and that of the gas core within the vortex chamber of the injector element. The difference in densities was found to excite flow instabilities in the internal swirling film. The local film thickness at the point of injection was shown to be highly dependent on such flow instabilities; therefore, it was shown that θ was directly related to variations in chamber pressure. Although correlating measurements of h were not made in this current study, the

spray angle analysis results coincide with, and seem to support, previous bodies of work.

Furthermore, measurements of θ were not observed to correspond with classical swirl injector design theory. For the nominal chamber pressure condition, a 7.3% discrepancy was measured. Based on inviscid assumptions, the injector design theory relies on the specification of a desired pressure drop across the injector to derive physical dimensions; if such a pressure drop is not conserved, θ cannot be conserved.

Comparison of stroboscopic imaging highlighted a qualitative view of sheet penetration length as chamber pressure increases. Through analysis, it was found that the κ decreases with a rise in chamber pressure conditions. Figure 4.4 highlights the aerodynamic effects that change in chamber pressure imposes on the swirling sheet. It was shown that, for steady mass flow rate conditions, surface tension is a key fluid property to the disintegration of the swirling sheet; surface tension is the only restorative force that acts to hold the sheet together. Primarily a function of temperature, the surface tension of water can be assumed to be constant with pressure, therefore negligible — leaving gas density as one of two major contributors to We_a. Thus We_a is directly proportional to gas density and inversely proportional to κ. However, it must be noted that $\boldsymbol{h}$ was empirically calculated via relations rooted in inviscid flow theory. Such a relation may not accurately reflect the aforementioned findings of Kenny.

5.2 Atomization Assessment

Analysis of the PDPA data yielded both key and auxiliary results pertaining to the self-atomizing behavior of the spray and to droplet flow dynamics. The observation of a recirculation zone within the hollow spray cone, indicated in Figure 4.13, seems to concur with observations and conclusions first made by DeCorso and Kemeny [21]. The recirculation zone creates a lowered static pressure that induces flow through the spray's boundary. In turn, it is thought that the induced flow increases aerodynamic drag on the sheet, thereby serving to enhance atomization. The measured negative velocities appear to support the theory that small droplets became entrained in the recirculation zone, whereby axial velocity vectors were decreased until turning negative near the spray center.

The skewed nature of the diameter distribution histograms in Figure 4.12 corresponds with classic atomization theory outlined by Lefebvre [16]. Several emperical models, based on the standard log-normal statistical distribution, exist to describe the distribution of droplet measurements, notably the Rossin-Rammler and the Nukiyama-Tanasawa. Qualitatively, results seem to suggest that a single droplet distribution model does not effectively describe all regions of the flow throughout the profile of the spray envelope — that the distribution shape has a spatial dependence. Further analysis is required to determine if a new emperical fit can

best describe droplet distributions in the spray or if existing models are appropriate.

Figure 4.20 and Figure 4.21 highlight the effects of chamber pressure on droplet velocity in the spray's primary atomization zone. Furthermore, Figure 4.22 and Figure 4.23 capture the influence of chamber pressure on droplets in the bulk flow. For both flow properties, positive variation in chamber pressure had a general diminishing effect. From a droplet aerodynamics approach, this observation is intuitive; as gas density increases, drag will increase. Such drag overcomes the surface tension of the droplet, promoting further atomization until droplet momentum and surface tension reach equilibrium. However, a droplet aerodynamics approach does not explain the connection between chamber pressure variation and injector self-atomization, but merely provides a metric for evaluation.

To fully investigate the influence of chamber pressure on swirl injector self-atomization, the dynamics of the continuum flow must be scrutinized and aerodynamic drag experienced by the flow identified. To compute drag, the geometry of the conical sheet must be known. Although imaging can resolve the length of the cone, additional information pertaining to the thickness and taper of the film is needed. The relationship between chamber density and h has been established [5], but to link chamber density to variations in droplet flow properties, h must be related to the velocities and diameters of the bulk flow droplets in the primary atom-

ization region. The dynamic behavior of the film's taper must be explored as a function of initial h conditions — as dictated by chamber density.

5.3 Recommendations

Although this study was successful in the characterization of swirl injector behaviors at real LPRE operating conditions, the effort was a characterization of *fundamental* injection processes. To assess injector performance in an applications approach, co-flow from the outer fuel annulus must be supplied. The interaction of the outer liquid jet with the inner swirling liquid sheet cannot be neglected, as the entire flow field will be altered. The impingement of the jet with the sheet will dramatically enhance spray atomization qualities of the injector.

Several improvements to the experimental approach and methodologies can be implemented. At the core of the cold flow approach was the isolation of injector fluid mechanics from combustion processes. Injection and atomization can be separated from combustion; however, the effects of combustion cannot be neglected. Experimental techniques should be made to include mechanisms of rapid gas expansion created by the combustion process to better simulate an imparted turbulence on the spray.

H_2O is an effective simulant for LOX in regards to the study of continuum fluid mechanics such as the internal flow of the injector. However, the fluid property that exerts the most influence on atomization — sur-

face tension — is significantly dissimilar between LOX and water for an effective study of spray break-up, unless We is conserved. Nevertheless, if matching of non-dimensional flow parameters is not practiced, the fluid properties of H_2O should be artificially altered with temperature variation, surfactants, and/or alcohol or glucose-based additives. Alternatively, an inert simulant to replace water, such as LN_2, should be selected.

An effective method to quantify the uncertainty associated with PDPA droplet diameter measurements should be devised and implemented. Although the instrument is manufacturer-calibrated, such a standard does not remove systematic biases potentially introduced by device settings and flow conditions. To account for these forms of systematic uncertainty, PDPA measurements should be independently calibrated against a monodispersed droplet size test while using anticipated device settings.

APPENDICES

APPENDIX A

HIGH PRESSURE SPRAY FACILITY COMPONENTS

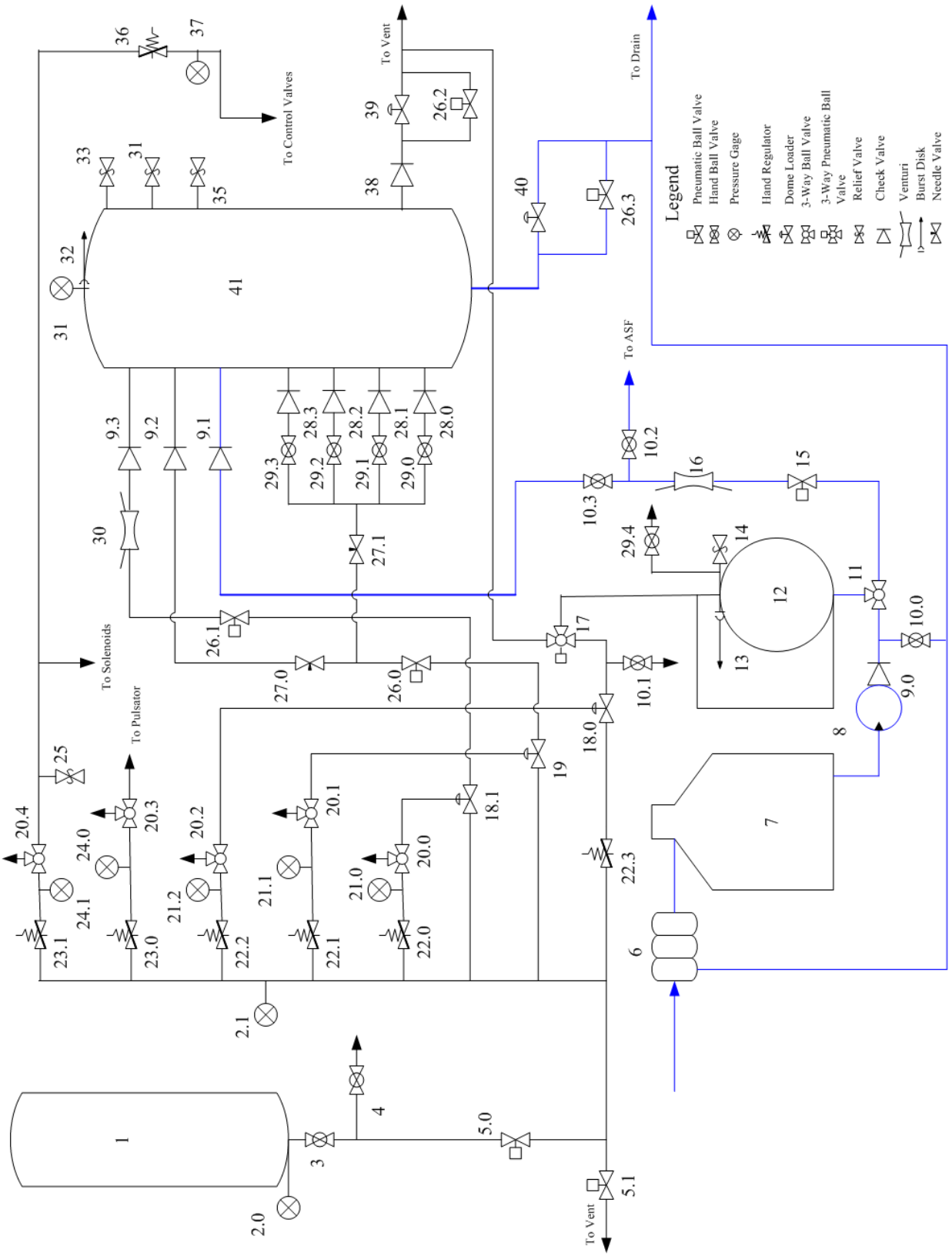

Figure A.1: Piping and Intrumentation Diagram of the High Pressure Spray Facility

Table A.1: High Pressure Spray Facility Components List

Call-out	Description	Manufacturer	Model
1	500 ft^3, 3000 psig	N/A	N/A
2.0	0-4000 psig	Helicold	N/A
2.1	0-4000 psig	Helicold	N/A
3	1", 5000 psig	Hylok	N3B-H-16TPC
4	$\frac{1}{2}$"	Parker	N/A
5.0	1", 2500 psig	Swagelok	N/A
5.1	1", 2500 psig	Swagelok	N/A
6	300 $\frac{gal}{day}$	AquaFX	N/A
7	300 gal	Ace	N/A
8	$\frac{1}{10}$ HP	Little Giant	977442 E40513
9.0	$\frac{1}{2}$", $\frac{1}{3}$ psia	Hylok	CVH2-H8T-1-S316
9.1	$\frac{1}{2}$", $\frac{1}{3}$ psia	Hylok	CVH2-H8T-1-S316
9.2	$\frac{1}{2}$", $\frac{1}{3}$ psia	Hylok	CVH2-H8T-1-S316
9.3	$\frac{1}{2}$", $\frac{1}{3}$ psia	Hylok	CVH2-H8T-1-S316
10.0	$\frac{1}{2}$"	Hylok	H1B-H-8TPC
10.1	$\frac{1}{2}$"	Hylok	H1B-H-8TPC
10.2	$\frac{1}{2}$"	Hylok	H1B-H-8TPC
10.3	$\frac{1}{2}$"	Hylok	H1B-H-8TPC
11	$\frac{1}{2}$"	Hylok	H1B3B-H8TPC
12	60 gal, 2000 psig	Prentex	D220 2007
13	$\frac{1}{2}$", 2100 psig	Fike	SCRD
14	$\frac{1}{2}$", 1500-2250 psig	Hylok	RV2MH-8N8T-C-S316
15	$\frac{1}{2}$"	Parker	8A-B8XJ2-V-SS-61ADX
16	$\frac{1}{2}$", variable area	Fox Valve	N/A
17	$\frac{1}{2}$"	Parker	8A-B8XJ2-V-SS-61ADX
18.0	$\frac{1}{2}$", 0-6000 psig	Tescom	26-1111-282
18.1	$\frac{1}{2}$", 0-6000 psig	Tescom	26-1111-282
19	$\frac{3}{4}$", 0-10000 psig	Tescom	26-1221-212
20.0	$\frac{1}{4}$"	Hylok	H1B3S-H4TPC
20.1	$\frac{1}{4}$"	Hylok	H1B3S-H4TPC

Table A.2: HiPSF Components List Continued

Call-out	Description	Manufacturer	Model
20.2	$\frac{1}{4}$"	Hylok	H1B3S-H4TPC
20.3	$\frac{1}{4}$"	Hylok	H1B3S-H4TPC
20.4	$\frac{1}{4}$"	Hylok	H1B3S-H4TPC
21.0	0-3000 psig	Omega	PMG-100L-3000
21.1	0-3000 psig	Omega	PMG-100L-3000
21.2	0-3000 psig	Omega	PMG-100L-3000
22.0	0-2500 psig	Tescom	26-1064-24
22.1	0-2500 psig	Tescom	26-1064-24
22.2	0-2500 psig	Tescom	26-1064-24
23.0	0-500 psig	Tescom	26-1016-24
23.1	0-500 psig	Tescom	26-1016-24
24.0	0-600 psig	Omega	PMG-100L-600
24.1	0-600 psig	Omega	PMG-100L-600
25	$\frac{1}{4}$", 10-250 psig	Hylok	RV1MF-4N-S316
26.0	$\frac{3}{4}$"	Parker	12A-B8LJ2-SS-62AC-3
26.1	$\frac{3}{4}$"	Parker	12A-B8LJ2-SS-62AC-3
26.2	$\frac{3}{4}$"	Parker	12A-B8LJ2-SS-62AC-3
26.3	$\frac{3}{4}$"	Parker	12A-B8LJ2-SS-62AC-3
27.0	$\frac{1}{2}$"	Hylok	NV4H-8T-S316
27.1	$\frac{1}{2}$"	Hylok	NV4H-8T-S316
28.0	$\frac{1}{4}$", $\frac{1}{3}$ psia	Hylok	CVH2-H4T-1-S316
28.1	$\frac{1}{4}$", $\frac{1}{3}$ psia	Hylok	CVH2-H4T-1-S316
28.2	$\frac{1}{4}$", $\frac{1}{3}$ psia	Hylok	CVH2-H4T-1-S316
28.3	$\frac{1}{4}$", $\frac{1}{3}$ psia	Hylok	CVH2-H4T-1-S316
29.0	$\frac{1}{4}$"	Swagelok	SS43GS4
29.1	$\frac{1}{4}$"	Swagelok	SS43GS4
29.2	$\frac{1}{4}$"	Swagelok	SS43GS4
29.3	$\frac{1}{4}$"	Swagelok	SS43GS4
30	$\frac{3}{4}$", fixed area	Fox Valve	N/A
31	0-600 psig	Duraguage	N/A

Table A.3: HiPSF Components List Continued

Call-out	Description	Manufacturer	Model
32	1”, 656 psig	Fike	SRX
33	1”, 580 psig	Hydroseal	4FRV3LF/D5
34	$\frac{1}{4}$”, 225-750 psig	Hylok	RV2MF-4N-A-S316
35	$\frac{1}{4}$”, 350-750 psig	Swagelok	SS-4R3A5
36	$\frac{1}{8}$”, 0-50 psig	Porter	N/A
37	0-100 psig	U.S. Gage	SS-12C-10
38	$\frac{3}{4}$”, 10 psia	NUPRO	N/A
39	1-$\frac{1}{4}$”	Jordan Valve	MK708SP-075-S6/PT
40	$\frac{3}{4}$”	Jordan Valve	7J2728 2008
41	625 psig	Addison	N/A

APPENDIX B

DROPLET PROPERTY MAPS

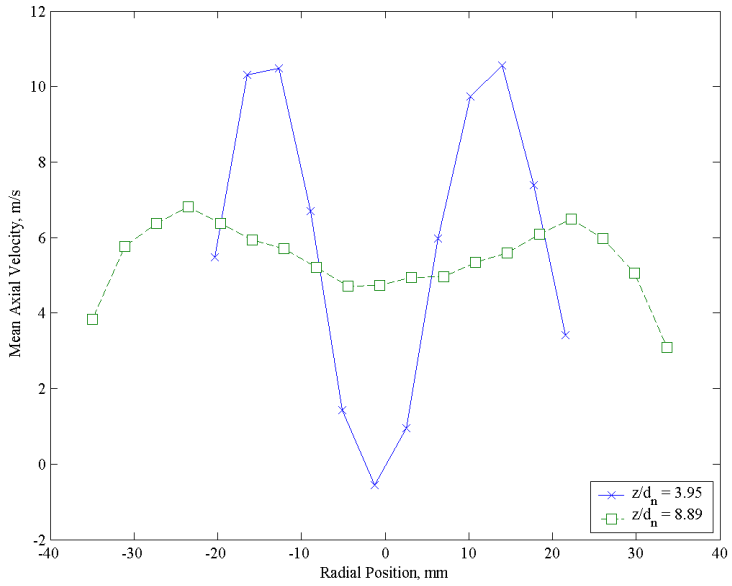

Figure B.1: Mapping of Droplet Mean Axial Velocity at $PR = 0.50$

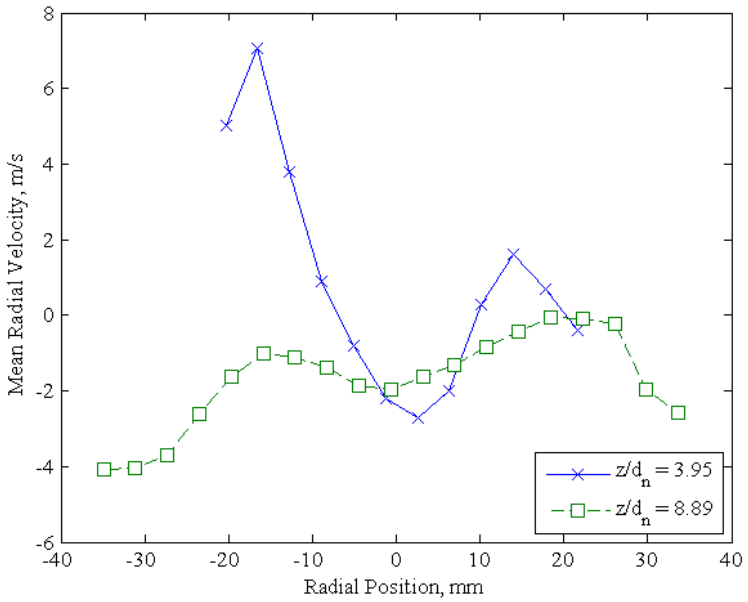

Figure B.2: Mapping of Droplet Mean Radial Velocity at $PR = 0.50$

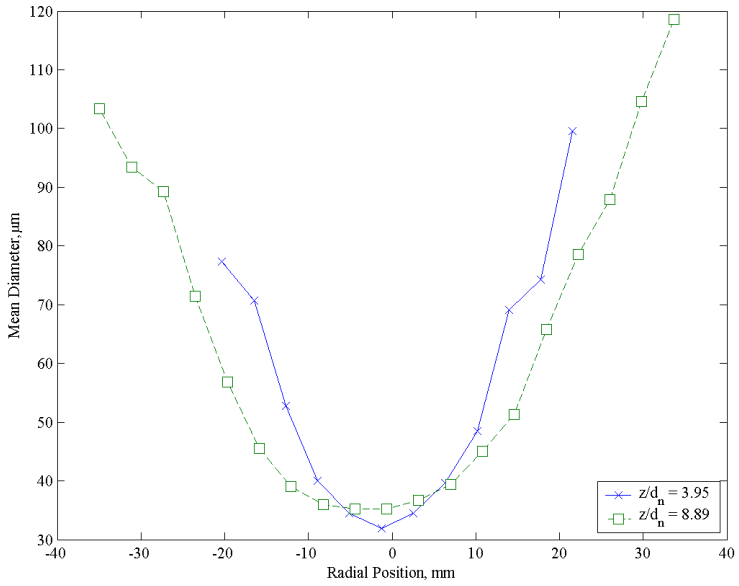

Figure B.3: Mapping of Droplet Mean Diameter at $PR = 0.50$

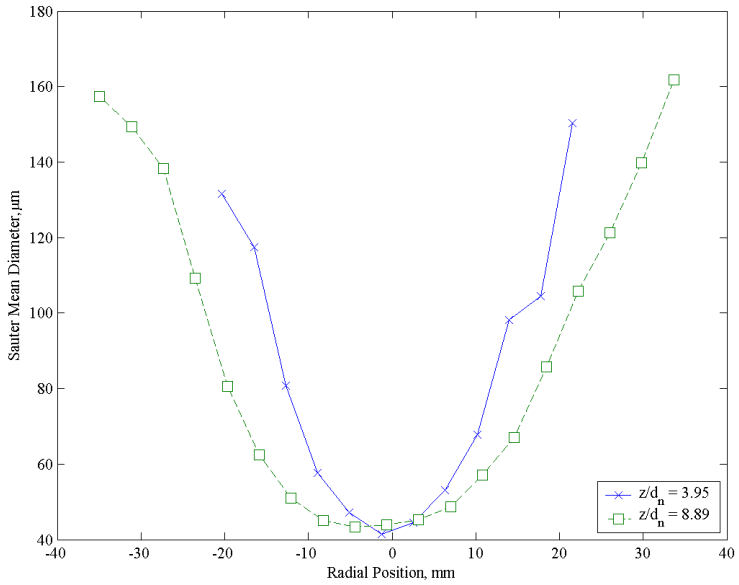

Figure B.4: Mapping of Droplet Sauter Mean Diameter at $PR = 0.50$

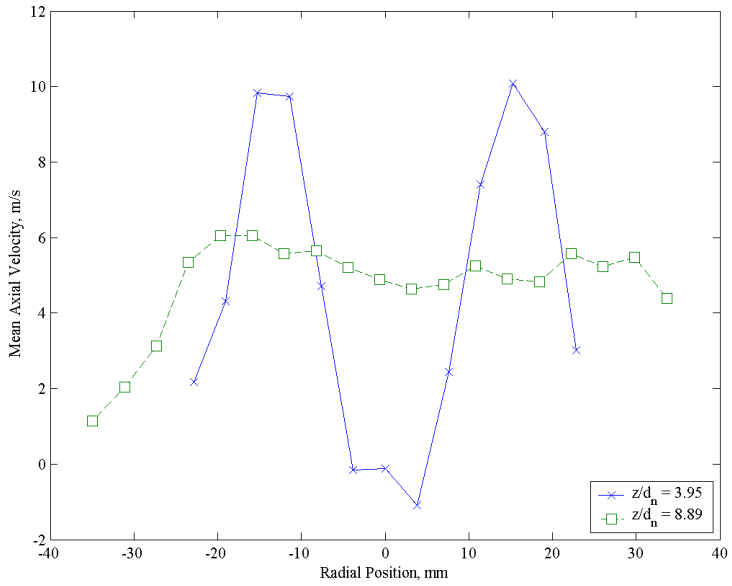

Figure B.5: Mapping of Droplet Mean Axial Velocity at $PR = 0.65$

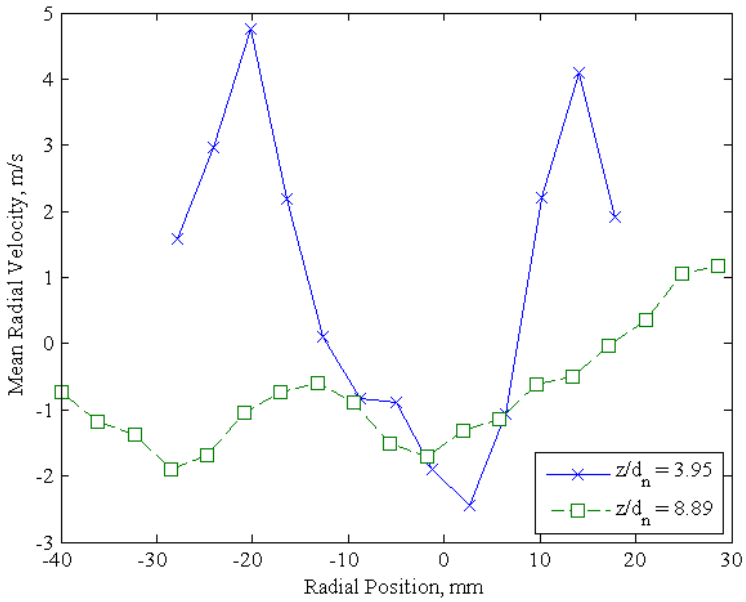

Figure B.6: Mapping of Droplet Mean Radial Velocity at $PR = 0.65$

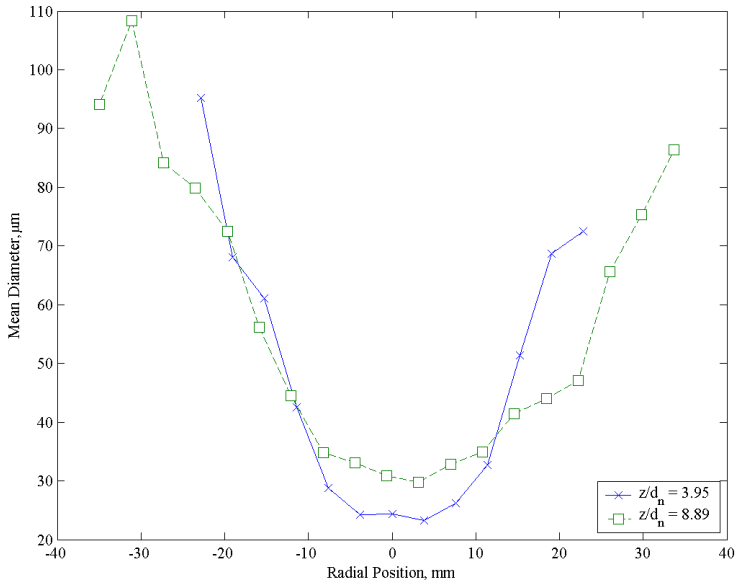

Figure B.7: Mapping of Droplet Mean Diameter at $PR = 0.65$

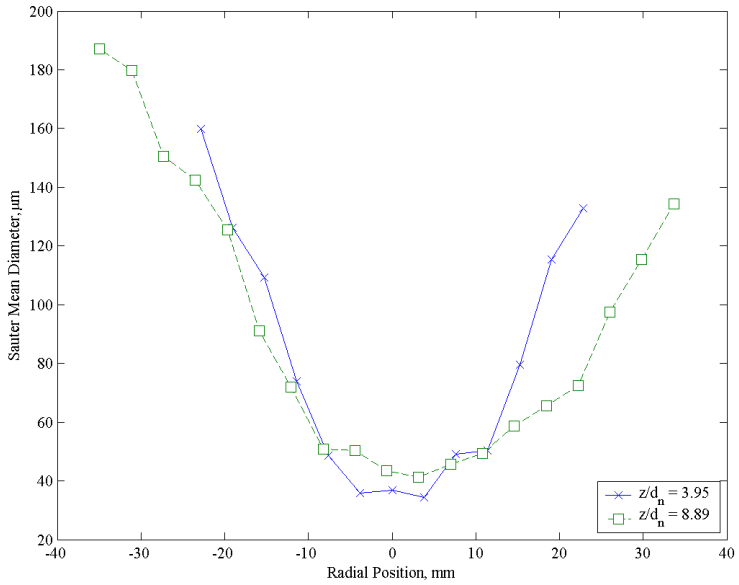

Figure B.8: Mapping of Droplet Sauter Mean Diameter at $PR = 0.65$

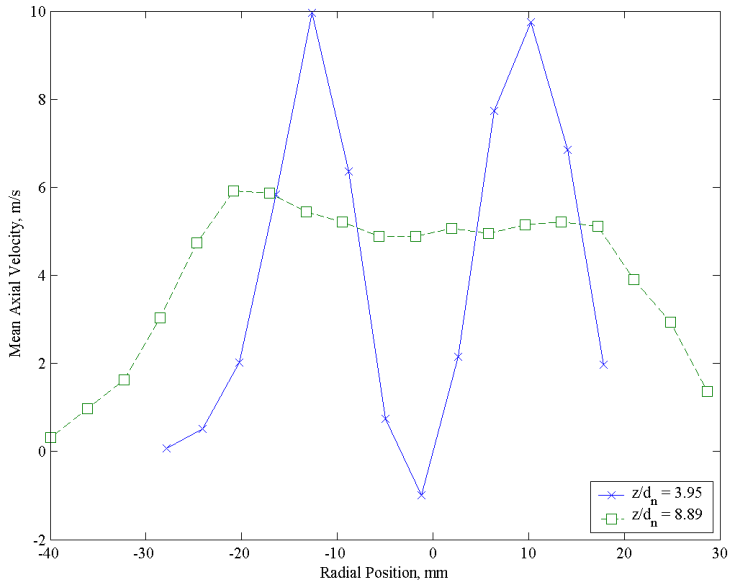

Figure B.9: Mapping of Droplet Mean Axial Velocity at $PR = 0.85$

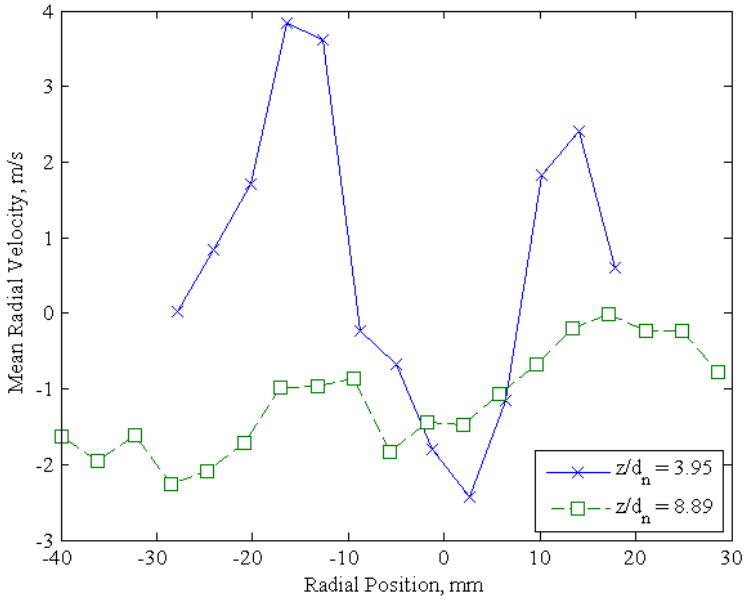

Figure B.10: Mapping of Droplet Mean Radial Velocity at $PR = 0.85$

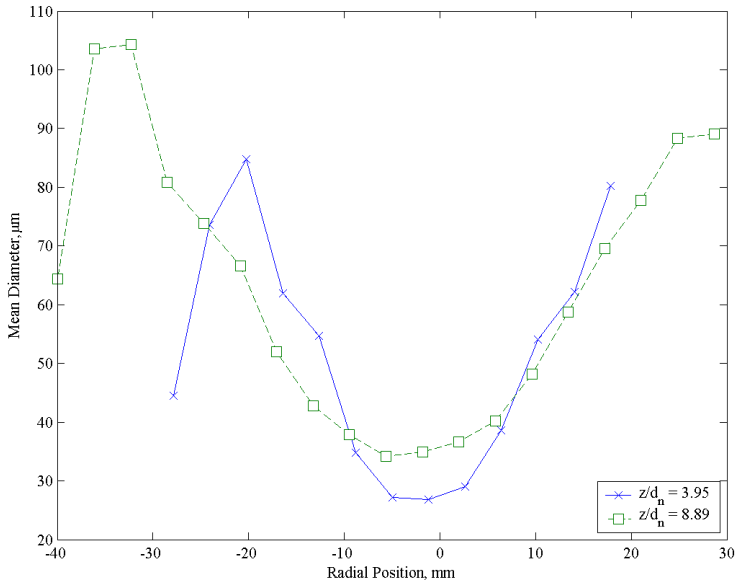

Figure B.11: Mapping of Droplet Mean Diameter at $PR = 0.85$

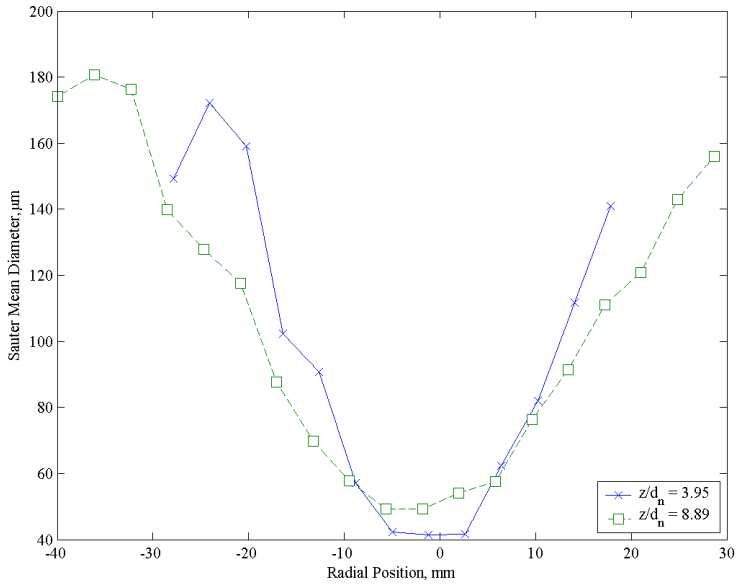

Figure B.12: Mapping of Droplet Sauter Mean Diameter at $PR = 0.85$

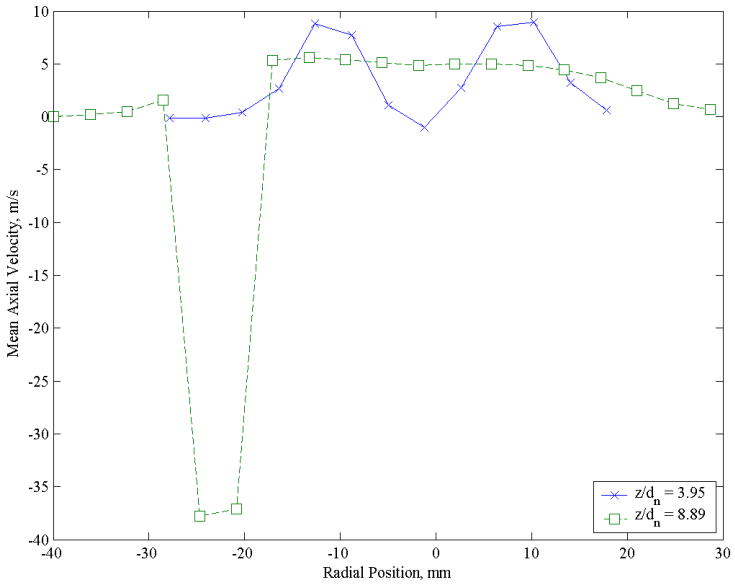

Figure B.13: Mapping of Droplet Mean Axial Velocity at $PR = 1.15$

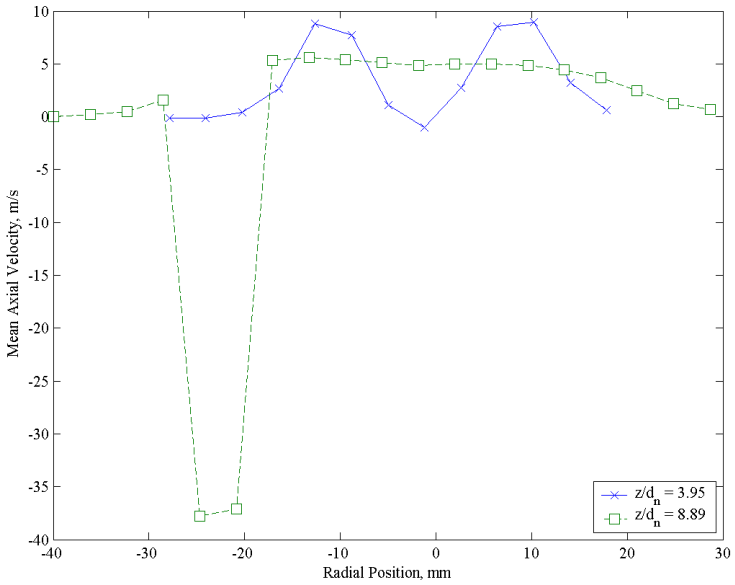

Figure B.14: Mapping of Droplet Mean Radial Velocity at $PR = 1.15$

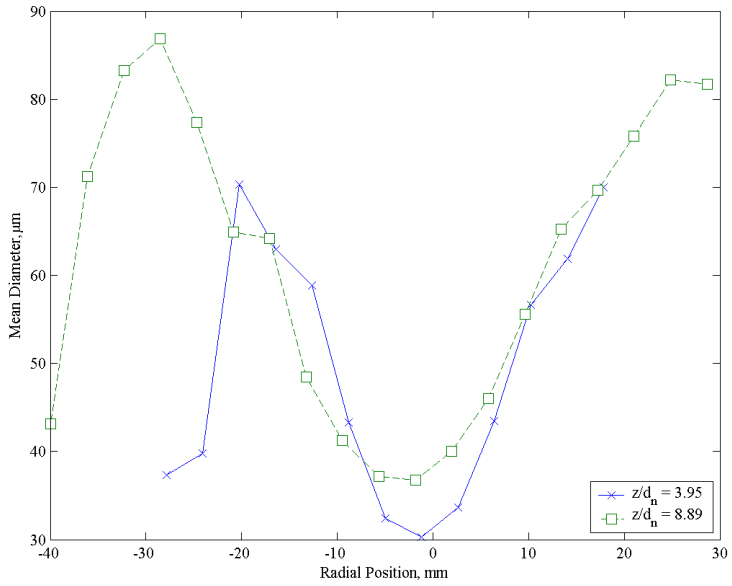

Figure B.15: Mapping of Droplet Mean Diameter at $PR = 1.15$

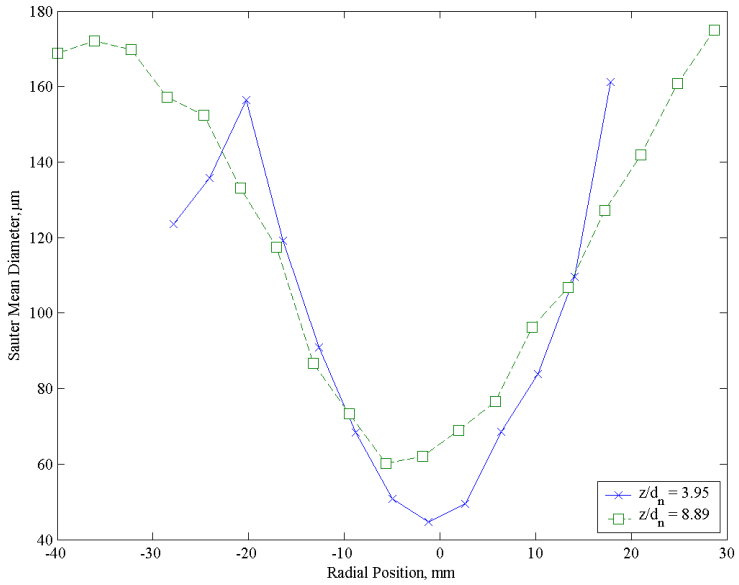

Figure B.16: Mapping of Droplet Sauter Mean Diameter at $PR = 1.15$

APPENDIX C

DROPLET AXIAL VELOCITY VECTOR FIELDS AND DIAMETERS

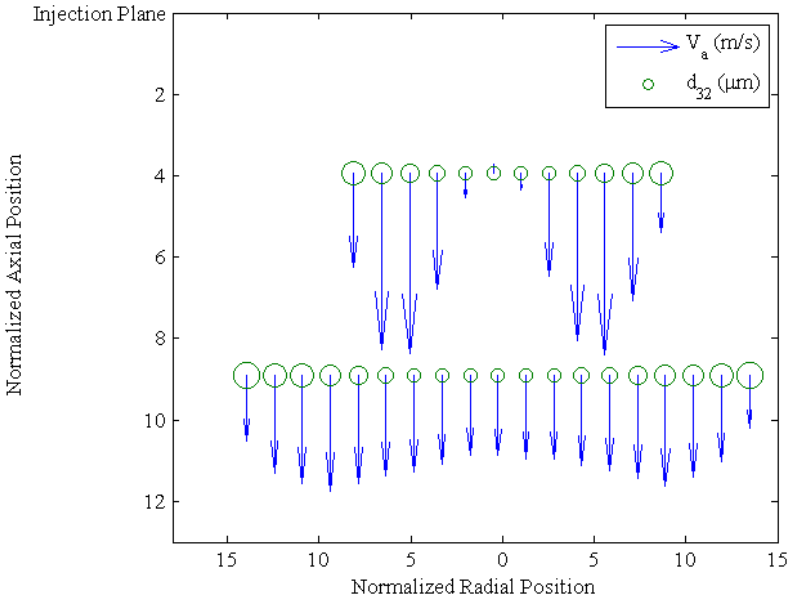

Figure C.1: Axial Flow Field and Diameters of Droplets at $PR = 0.50$

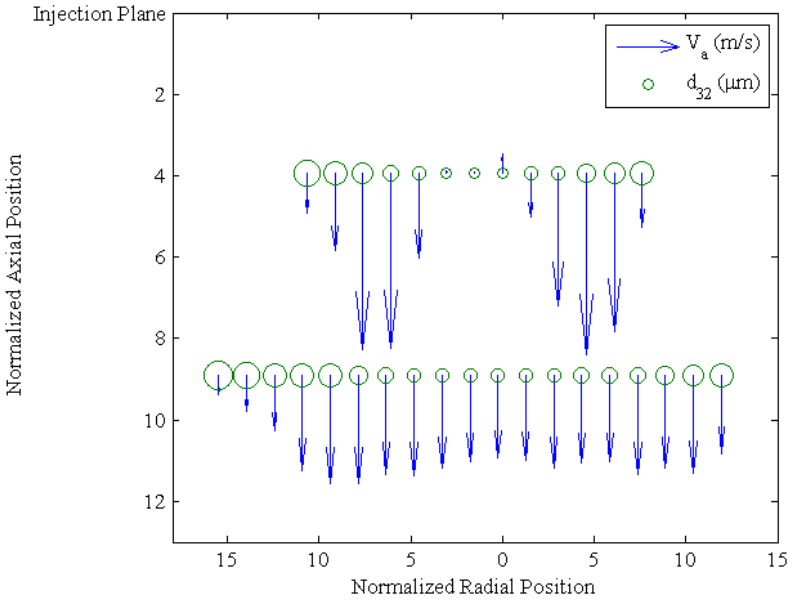

Figure C.2: Axial Flow Field and Diameters of Droplets at $PR = 0.65$

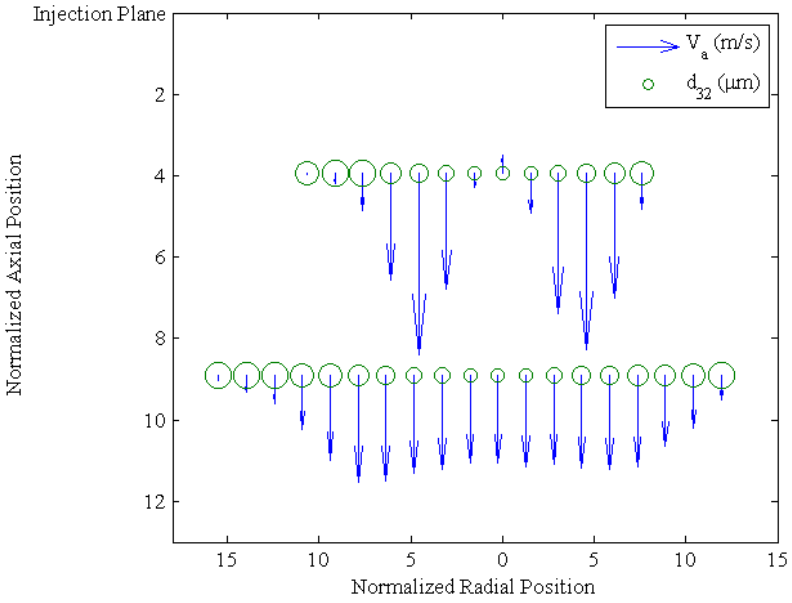

Figure C.3: Axial Flow Field and Diameters of Droplets at $PR = 0.85$

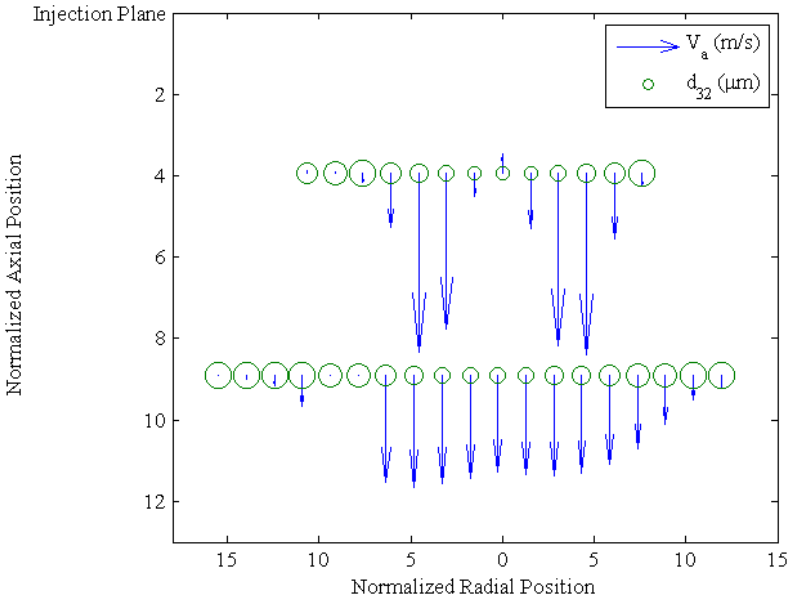

Figure C.4: Axial Flow Field and Diameters of Droplets at $PR = 1.15$

APPENDIX D

DIAMETER DISTRIBUTION PROFILES IN THE PRIMARY ATOMIZATION ZONE

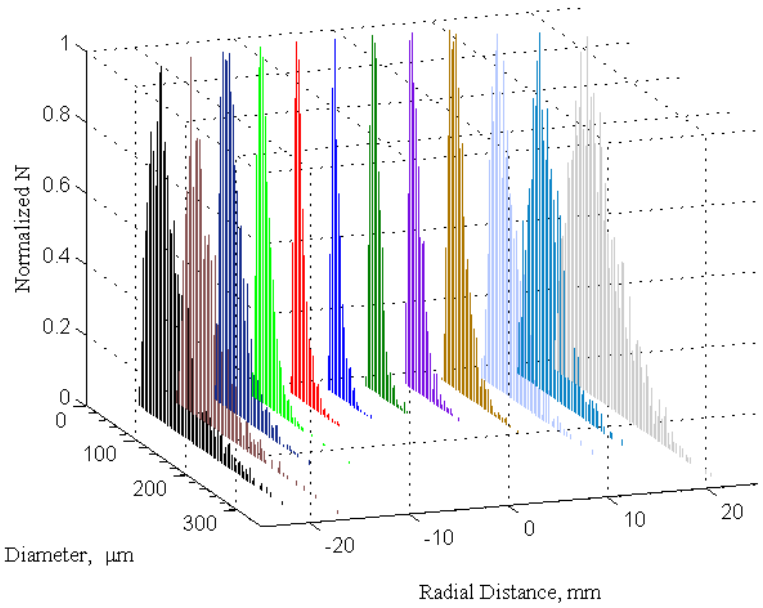

Figure D.1: Diameter Distribution Profile Mapping at $PR = 0.50$

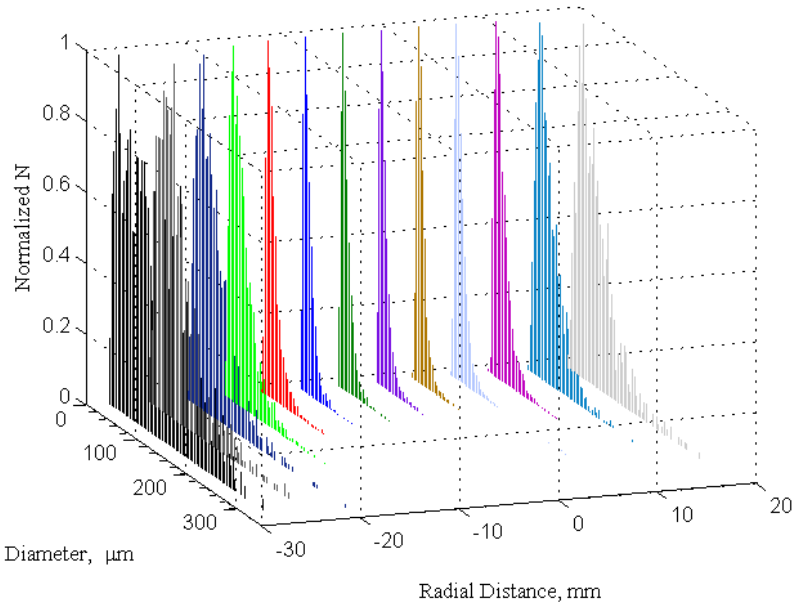

Figure D.2: Diameter Distribution Profile Mapping at $PR = 0.65$

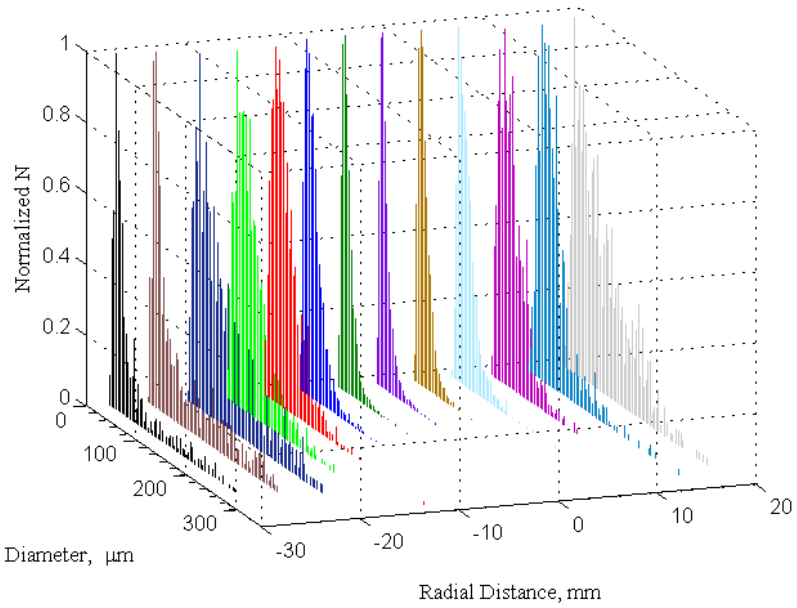

Figure D.3: Diameter Distribution Profile Mapping at $PR = 0.85$

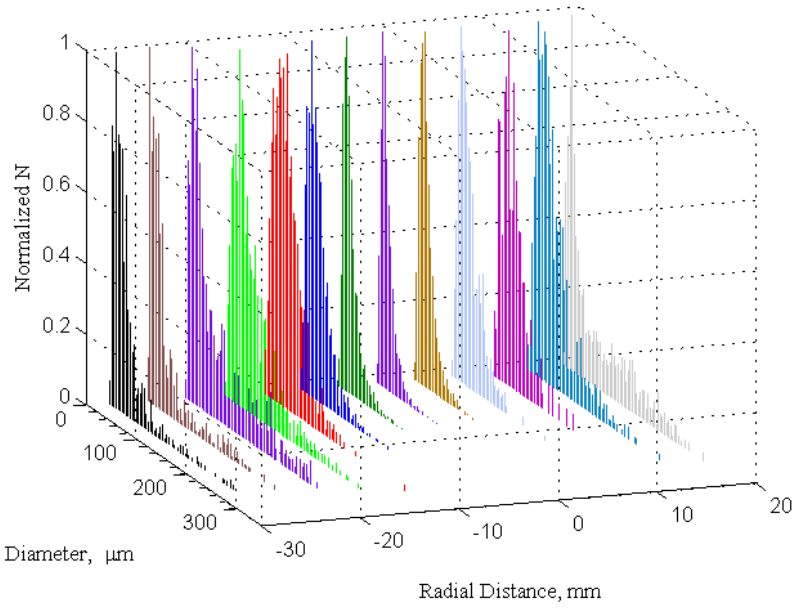

Figure D.4: Diameter Distribution Profile Mapping at $PR = 1.15$

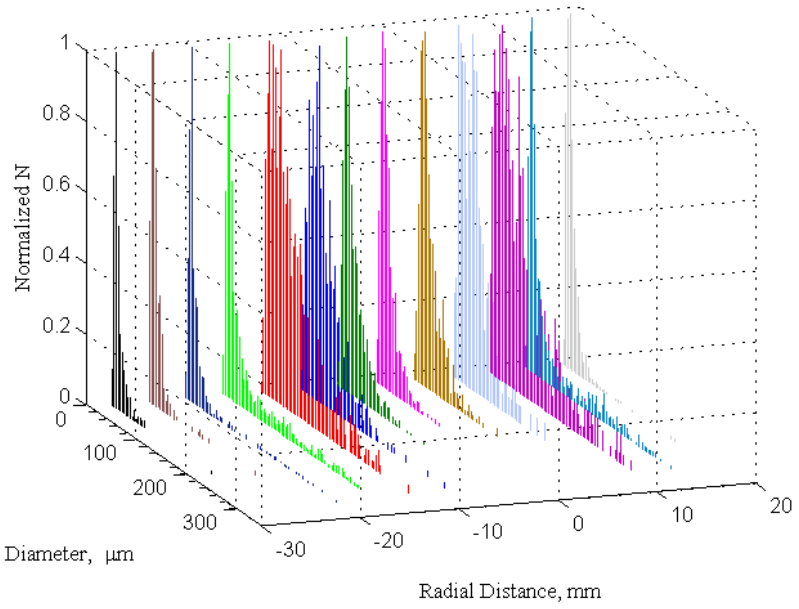

Figure D.5: Diameter Distribution Profile Mapping at $PR = 1.82$

APPENDIX E

DROPLET MEASUREMENT COMPARISONS ON THE REFERENCE PLANE

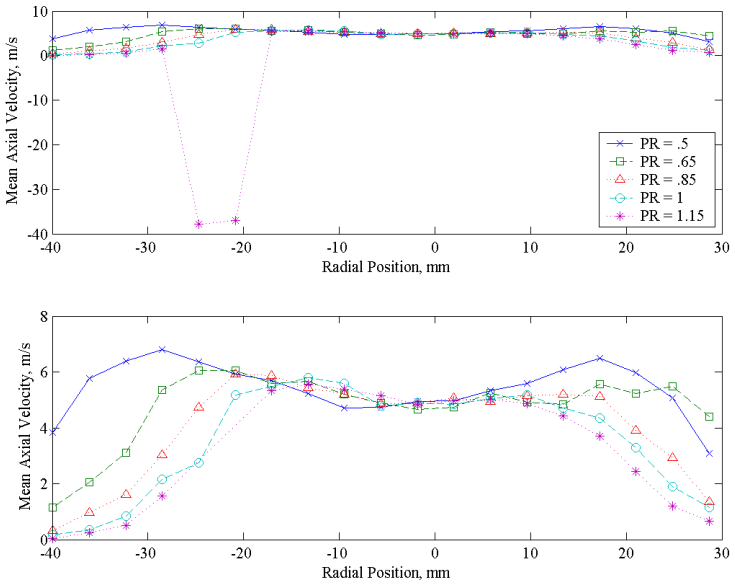

Figure E.1: Comparison of Mean Axial Velocity Profiles on the Reference Plane

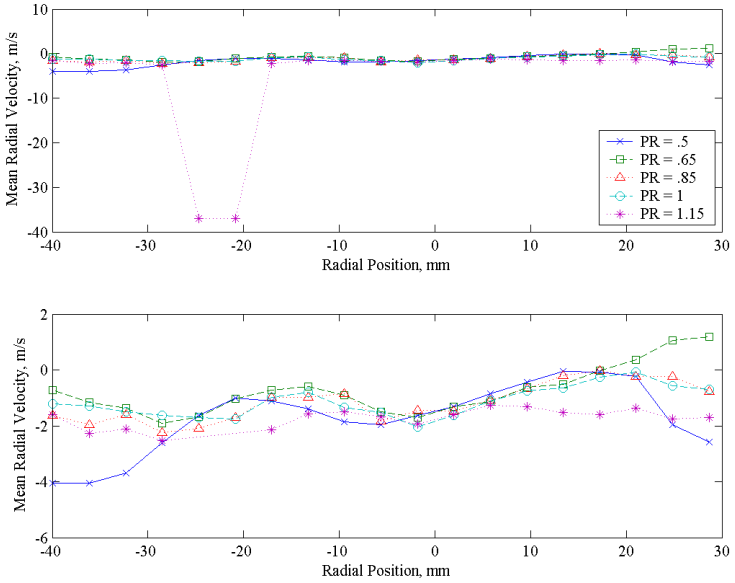

Figure E.2: Comparison of Mean Radial Velocity Profiles on the Reference Plane

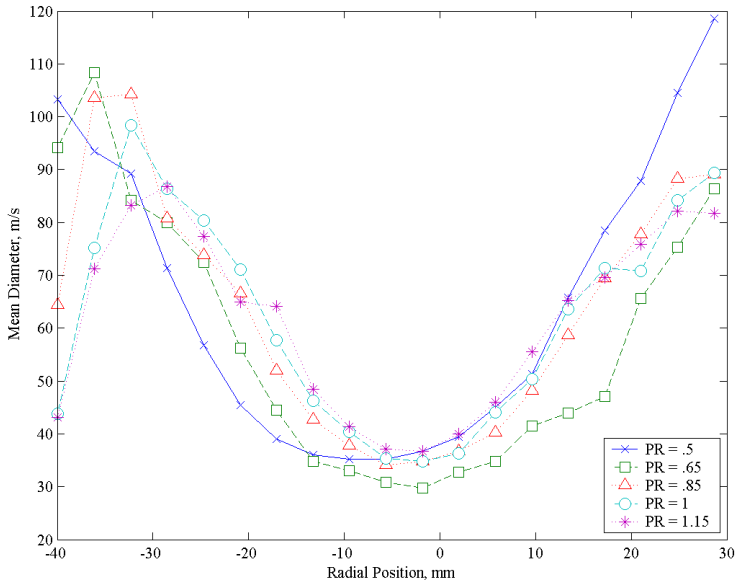

Figure E.3: Comparison of Mean Diameter Profiles on the Reference Planee

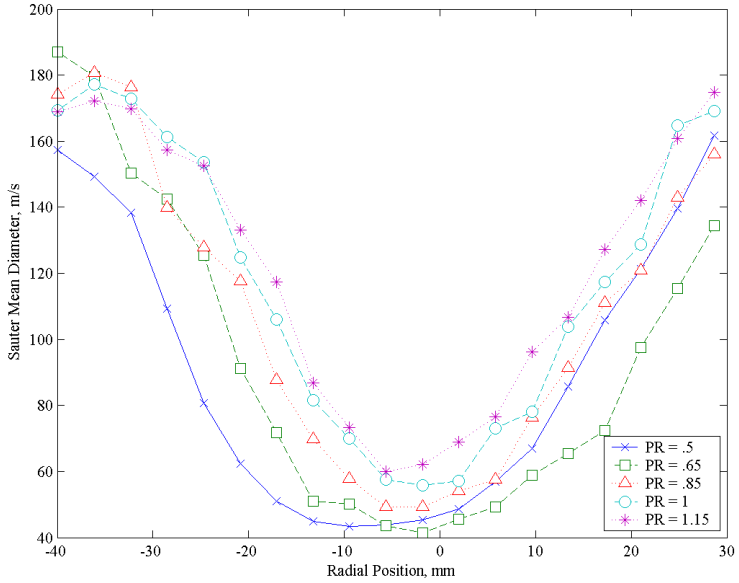

Figure E.4: Comparison of Sauter Mean Diameter Profiles on the Reference Plane

REFERENCES

[1] J.R. Hulka. Scaling of Performance in Liquid Propellant Rocket Engine Combustion Devices. In 44^{th} ***AIAA/ASME/SAE/ASEE Joint Propulsion Conference***, number AIAA 2008-5113, Hartford, CT, 2008. American Institute of Aeronautics and Astronautics.

[2] R.J. Kenny, M.D. Moser, J.R. Hulka, and G. Jones. Cold Flow Testing for Liquid Propellant Rocket Injector Scaling and Throttling. In 42^{nd} ***AIAA/ASME/SAE/ASEE Joint Propulsion Conference***, number AIAA 2006-4705, Sacramento, CA, 2006. American Institute of Aeronautics and Astronautics.

[3] C.E Dexter, M.F. Fisher, J.R. Hulka, K.P. Denisov, A.A. Shibanov, and A.F. Agarkov. Scaling Technologies for Design, Developement and Test. In V. Yang, M. Habiballah, J. Hulka, and M. Poppe, editors, ***Liquid Rocket Thrust Chambers: Aspects of Modeling, Analysis, and Design, Progress in Astronautics and Aeronautics, Vol. 200***, pages pp. 553–600. American Institute of Aeronautics and Astronautics, Washington, DC, 2004.

[4] G.B. Cox. Rocket Engine Injection Element Characterization. In 24^{th} ***AIAA/ASME/SAE Joint Propulsion Conference***, number AIAA 1988-3135, Boston, MA, 1988. American Institute of Aeronautics and Astronautics.

[5] R.J. Kenny. ***Influence of Variable Thrust Parameters on Swirl Injector Fluid Mechanics.*** Ph.d. dissertation, The University of Alabama in Hunstville, 2008.

[6] R.J. Kenny, J.R. Hulka, M.D. Moser, and N.O. Rhys. Effect of Chamber Backpressure on Swirl Injector Fluid Mechanics. ***Journal of Propulsion and Power***, 25(4):902–913, July 2009.

[7] D. Kim, P. Han, J. Im, P. Yoon, and V.G. Bazarov. Effect of Recess on the Spray Characteristics of Liquid-Liquid Swirl Coaxial Injectors. ***Journal of Propulsion and Power***, 23(6):1194–1203, Nov 2007.

[8] P.A. Strakey, D.G. Talley, and J.J. Hutt. Mixing Characteristics of Coaxial Injectors at High Gas/Liquid Momentum Ratios. ***Journal of Propulsion and Power***, 17(2):402–410, Mar 2001.

[9] M.R. Long, V.G. Bazarov, and W.E. Anderson. Main Chamber Injectors for Advanced Hydrocarbon Booster Engines*. In 39^{th} ***AIAA/ASME/SAE/ASEE Joint Propulsion Conference***, number AIAA 2003-4599, Huntsville, AL, 2003. American Institute of Aeronautics and Astronautics.

[10] Joseph Shakal. LDV and PDPA Training & Workshop- Lecture Notes. Technical report, TSI Incorporated, 2007.

[11] T.W. Lee. ***Thermal and Flow Measurements.*** 1^{st} edition.

[12] Specification for 5,500 $\pm$100 lb_f(vac) Engine Request for Proposal. Technical report, National Aeronautics and Space Administration, Glenn Research Center, Dec 2007.

[13] V. Bazarov, V. Yang, and P. Puri. Design and Dynamics of Jet and Swirl Injectors. In V. Yang, M. Habiballah, J. Hulka, and M. Poppe, editors, ***Liquid Rocket Thrust Chambers: Aspects of Modeling, Analysis, and Design, Progress in Astronautics and Aeronautics, Vol. 200***, pages pp. 19–103. American Institute of Aeronautics and Astronautics, Washington, DC, 2004.

[14] George P. Sutton and Oscar Biblarz. ***Rocket Propulsion Elements.*** 7^{th} edition.

[15] Hugh W. Coleman and Glenn W. Steele. ***Experimentation, Validation & Uncertainty Analysis for Engineers.*** 3^{rd} edition.

[16] Arthur H. Lefebvre. ***Atomization and Sprays.*** 1^{st} edition.

[17] William A. Sirignano. ***Fluid Dynamics and Transport of Droplets and Sprays.*** 1^{st} edition.

[18] J.R. Hulka and D. Makel. Liquid oxygen/Hydrogen Testing of a Single Swirl Coaxial Injector Element in a Windowed Combustion Chamber. In 29^{th} ***AIAA/ASME/SAE/ASEE Joint Propulsion Conference***, number AIAA 1993-1954, Monterey, CA, 1993. American Institute of Aeronautics and Astronautics.

[19] C.J. Eberhart, D.M. Lineberry, and M.D. Moser. Experimental Cold Flow Characterization of a Swirl Coaxial Injector Element. In 45^{th} ***AIAA/ASME/SAE/ASEE Joint Propulsion Conference***, number AIAA 2009-5140, Denver, CO, 2009. American Institute of Aeronautics and Astronautics.

[20] M. Suyari and A.H. Lefebvre. Film Thickness Measurements in a Simplex Swirl Atomizer. ***Journal of Propulsion and Power***, 2(6):528–533, Mar 2001.

[21] **S.M. DeCorso and G.A. Kemeny. Effect of Ambient and Fuel Pressure on Nozzle Spray Angle. In *ASME Gas Turbine Power Division Conference*, number ASME 1956-GTP-3, New York, NY, 1956. American Society of Mechanical Engineers.**